UNIVERSITY OF CALIFORNIA SAN DIEGO

Photonic Topological Insulators and their applications as Waveguides and Antennas

A dissertation submitted in partial satisfaction of the
requirements for the degree
Doctor of Philosophy

in

Electrical Engineering (Applied Electromagnetics)

by

Shreya Singh

Committee in charge:

Professor Dan Sievenpiper, Chair
Professor Prabhakar Bandaru
Professor Michael Fogler
Professor Eric Fullerton
Professor Zhaowei Liu

2021

The dissertation of Shreya Singh is approved, and it is acceptable in quality and form for publication on microfilm and electronically.

University of California San Diego

2021

DEDICATION

To my parents Manoj and Meera, and my sister Tanya

EPIGRAPH

No day is so bad

it can't be fixed with a nap.

—Carrie Snow

TABLE OF CONTENTS

LIST OF FIGURES

LIST OF TABLES

ACKNOWLEDGEMENTS

Graduate school has been an incredibly journey with great intellectual and personal discovery. The naïve 21-year-old who flew over 8,000 miles away from home, to the opposite side of the globe, could never have even comprehended what the next five years would have in store. It has taken the love, support and care of almost a small village's worth of people for me to have reached this point of being able to write a doctoral dissertation.

Firstly, I would like to thank my advisor Dr. Dan Sievenpiper for his academic guidance and also for his patience and kindness in letting me work my way through the last five years at UC San Diego at my own, sometimes glacial, pace. I would like to thank each member of my dissertation committee: Prof. Eric Fullerton, Prof. Zhaowei Liu, Prof. Prabhakar Bandaru, and Prof. Michael Fogler, for their valuable suggestions and their time.

The biggest thanks goes to all the members, past and present, of the Applied Electromagnetics lab. To Dr. Dia'aaldin Bisharat, thank you for always pushing me to do my best, helping me learn, and being a great mentor. This Ph.D. would not have happened without you. To Dr. Jiyeon Lee, thank you for taking me under your wing and being my family. Your humility, generosity, and kindness humbles me, and I will always treasure our interactions and meme sharing. Thank you to Dr. Sanghoon Kim, Dr. Shiva Piltan, Dr. Aobo Li, Dr. Kyle Thackston (best desk buddy ever), Matt Smith (warmest and kindest human), Yun Zhou (joint favourite commiserator 1), Sara Kandil (joint favourite commiserator 2), Robert Davis (motivator extraordinaire), Erda Wen (insanely talented junior 1), and Xiaozhen Yang (insanely talented junior 2). The fates were smiling on the day I picked this lab. You are all some of the nicest people I've had the privilege of knowing. Regardless of how long or short our overlap in this lab has been, working with you all has truly been a source of unmitigated joy.

To the friends I've made in San Diego, thank you for the laughter, the hope and the shoulders to cry on. To Sonika Obheroi, for inspiring me to always put my best foot forward and for teaching me that its okay to not be a hermit because the outside world isn't all that scary.

To Vaishakh Ravi, for being my PhD and food buddy- San Diego would have been dreary and unexplored without you. To Ashwin Ramaswamy and Rishab Gulati, for being able to make me laugh at the drop of a hat.

I also owe thanks to the wonderful people who've mentored me while I was interning at Oracle Labs and Tesla Motors, especially, Dr. Aycan Erentok and Dr. Anand Konanur. Thank you for the summer of discovery and learning, and rekindled motivation.

My heartfelt love and gratitude to Sarthak Ahuja, Prateekshit Pandey, Chaitanya Kumar and Manan Gakhar. For having seen me at my best and at my worst for almost a decade and still choosing to love me. You've never failed to catch me during my falls, rejoice at my triumphs, challenge me intellectually, and make me want to be a better human being. I am eternally grateful for your lasting friendships.

A big thank you to all the artists, writers, poets, musicians, actors, and various other content developers who have created and curated the art that I enjoy, in all its many forms. It mesmerizes, inspires, invigorates, educates, evokes emotions, and makes me question what was, is and will be. Your art has sustained me through the toughest days of this journey.

And finally, to my beautiful and amazing family- Ma, Daddy and Didi. Thank you for the unwavering support and love. Thank you for your countless sacrifices, big and small. Thank you for always believing in me, even when I couldn't. But most importantly, thank you for always telling me that I can do it but even if I ever chose not to, I would always have a home to come back to. And that no matter what happened, you would always be proud of me. It means more than you can ever know. I love you.

Chapter 2 of this dissertation is based on Shreya Singh, Dia'aaldin Bisharat, and Dan Sievenpiper, "Spin-momentum locked interface modes based on transverse resonance and Zak phase in finite thickness dielectric slabs", *Under Submission*. The dissertation author was the primary author of this material.

Chapter 3 of this dissertation is based on Shreya Singh, Dia'aaldin Bisharat, and Dan

Sievenpiper, “Topological Antennas: Aperture Radiators,Leaky-wave Surfaces and Orbital Angular Momentum Beam Generation”, *Journal of Applied Physics*, 130(2):023101, 2021. The dissertation author was the primary author of this material.

Chapter 4 of this dissertation used materials from Shreya Singh, Dia’aaldin Bisharat, and Dan Sievenpiper, “Topological Antennas: Aperture Radiators, Leaky-wave Surfaces and Orbital Angular Momentum Beam Generation”, *Journal of Applied Physics*, 130(2):023101, 2021 **and** from Shreya Singh, Dia’aaldin Bisharat, and Dan Sievenpiper, “Generation and control of orbital angular momentum beams using metasurface photonic topological insulators”, *In Preparation*. The dissertation author was the primary author of this material.

VITA

2016	B. Tech. in Electronics and Communication Engineering *Gold Medal*, IIIT-Delhi, New Delhi, India
2021	Ph. D. in Electrical Engineering (Applied Electromagnetics), University of California San Diego, CA, USA

PUBLICATIONS

Shreya Singh, Dia'aaldin Bisharat, and Dan Sievenpiper, "Topological Antennas: Aperture Radiators, Leaky-wave Surfaces and Orbital Angular Momentum Beam Generation", *Journal of Applied Physics*, 130(2):023101, 2021.

Shreya Singh, Faisal Alsallum, Saud Saeed, Hatim Bukhari, and Dan Sievenpiper, "Analysis of Spatial and Frequency Proximity on Performance of Small Loop and Dipole Antennas", *IEEE Antennas and Wireless Propagation Letters*, 19(7):1266-1270, 2020.

Aobo Li, Shreya Singh, and Dan Sievenpiper, "Metasurfaces and their applications", *Nanophotonics*, 7(6):989-1011, 2019.

Shreya Singh, and P. B. Sujit, "Landmarks based path planning for UAVs in GPS-denied areas", *IFAC-PapersOnLine*, 49(1):396-400, 2016.

Shreya Singh, Dia'aaldin Bisharat, and Dan Sievenpiper, "Spin-momentum locked interface modes based on transverse resonance and Zak phase in finite thickness dielectric slabs", *Under Submission*.

Shreya Singh, Dia'aaldin Bisharat, and Dan Sievenpiper, "Generation and control of orbital angular momentum beams using metasurface photonic topological insulators", *In Preparation*.

Shreya Singh, Robert Davis, Dia'aaldin Bisharat, Jiyeon Lee, Sara Kandil, Era Wen, Xiaozhen Yang, Yun Zhou, Prabhakar Bandaru, and Dan Sievenpiper, "Advances in Metasurfaces: topology, chirality, patterning, and time modulation", *Under Submission*.

CONFERENCES and PRESENTATIONS

Shreya Singh, Dia'aaldin Bisharat, and Dan Sievenpiper, "Interface modes based on Zak phase for finite dielectric slabs (Conference Presentation)", *High Contrast Metastructures IX*. Vol. 11290. International Society for Optics and Photonics, 2020.

Dia'aldin Bisharat, Erda Wen, Sara Kandil, Xiaozhen Yang, Shreya Singh, Robert Davis, Yun Zhou, Prabhakar Bandaru, and Dan Sievenpiper, "Topological Metasurfaces", *2020 IEEE Asia-Pacific Microwave Conference (APMC)*, IEEE, 2020.

Dia'aldin Bisharat, Sara Kandil, Xianghong Kong, Shreya Singh, Zhixia Xu, and Dan Sievenpiper."Chiral and Topological Surface Waves and Line Waves on Metasurfaces", *Thirteenth International Congress on Artificial Materials for Novel Wave Phenomena (Metamaterials)*, pp. X-387. IEEE, 2019.

Shreya Singh, Faisal Alsallum, Saud Saeed, Hatim Bukhari, and Dan Sievenpiper,"Analysis of Multi-Antenna Proximity on Performance of Electrically Small Antennas", *2019 IEEE International Symposium on Antennas and Propagation and USNC-URSI Radio Science Meeting*, IEEE, 2019.

Shreya Singh, Pydi Bahubalindruni, and Joao Goes, "A robust fully-dynamic residue amplifier for two-stage SAR assisted pipeline ADCs", *2017 IEEE International Symposium on Circuits and Systems (ISCAS)*, IEEE, 2017.

Shreya Singh, and Mohammad S. Hashmi, "Exploring fractional order elements for single and dual band impedance matching for RF applications", *2016 International Conference on Signal Processing and Communications (SPCOM)*, IEEE, 2016.

ABSTRACT OF THE DISSERTATION

Photonic Topological Insulators and their applications as Waveguides and Antennas

by

Shreya Singh

Doctor of Philosophy in Electrical Engineering (Applied Electromagnetics)

University of California San Diego, 2021

Professor Dan Sievenpiper, Chair

Photonic topological insulators (PTIs) represent an area of emerging research into a new class of materials and devices with exciting electromagnetic properties. These materials are capable of supporting directional conducting modes along their surface or edge at frequencies that lie in the material bandgap. The presence of the bandgap ensures that the bulk of the material behaves as an insulator, which allows for a very high degree of energy confinement at the surface. This work briefly details a few variations on PTIs and then proceeds to focus on the creation of interface modes for 3D dielectric structures using only a 1D integration technique to obtain the geometric phase that is required for a material to be classified as topological. This 1D Zak phase allows for a simpler method to create topological waveguides with propagation path bends

in fixed directions, along with a directional dependence based on the rotational nature of the fields. A shift towards more traditional forms of PTIs in the latter half of the thesis focuses on the application aspects of topological insulators. The use of metallic spin PTI metasurfaces as antennas been demonstrated with device operation broken down into 1) confined and 2) leaky wave propagation. While the confined mode is best known for its use as energy guiding structures, abrupt truncations can allow for radiation at the aperture with a 'self-matched' property, allowing for immunity to the reflection caused due to the aperture impedance mismatch. Operation of the same PTI structure above the light cone in its leaky region enables the use of the PTI metasurface as a leaky wave antenna having an azimuth phase variation, with energy wrapped around in a closed loop propagation path. These waves possess an inherent orbital angular momentum (OAM), and control of the OAM beam charge can be achieved by the manipulating the physical and electrical path lengths. This control is invaluable to switching and multiplexing of different beam orders, which has a pivotal role to play in affecting the channel capacity and increasing data transmission rates for communication systems, among other important applications.

Chapter 1

Introduction to Photonic Topological Insulators

1.1 Topological Insulators

Topological insulators or TIs represent an area of relatively new, varied, and extensive research into specialized materials that are insulating in their bulk but conducting along a surface or an edge. The first half of the word, 'topology' comes from mathematics and is based on how certain geometric properties of materials are preserved under continuous deformations such as twisting, bending and stretching. Homotopy and homology are two forms of topological equivalence wherein structures are classified based on the number of 'holes' in them. Materials having the same number of holes that can be smoothly deformed from one shape to another and back are considered topologically equivalent. Figure 1.1 shows an example of topologically equivalent materials.

In physics and engineering, the arrangement of atoms or similar such elementary particles that make up a material or device, play a vital role in characterizing many physical properties such as conductivity, tensile strength, stiffness, friction, etc. Materials that may appear very dissimilar

Figure 1.1: Topological equivalence based on the number of holes in each object. Members of the same class can be smoothly deformed from one shape to another and back without having to make any cuts or incisions. Converting a doughnut hole (holes=0) into a coffee mug (holes=1) would required an incision to create a through-and-through hole for the mug handle and therefore, these materials are not topologically equivalent.

but are topologically equivalent can share similarities in these physical parameters [1, 2].

The latter half of the term, 'insulator' simply refers to materials that prohibit the conduction of energy. They can be phononic, electronic, or photonic and are often characterized by a gap between the conduction and valence states, commonly referred to as a band gap. Since the transmission of energy through the body of the material is forbidden in such a band gap, they are referred to as insulators.

So put together, a topological insulator refers to a material with some specific geometric/topological properties that acts as a specialized insulator. The bulk/inside of these materials acts as an ordinary insulator with a normal bandgap but on the edges or surfaces of these materials, special conducting states that pop up in the bandgap can be found. The energy in these conducting states is tightly confined to the surface of the material, can propagate unidirectionally, and is extremely robust owing to the topological properties of the material. The robustness implies a strong resistance to scattering from fabrication defects, structural impurities, and even sharp bends in the propagation path. In general, TIs are constructed of periodic or pseudo-periodic

lattices, like molecules (in condensed matter physics for electronic systems) or metamaterials (for phononic and photonic systems).

While detailing the physics behind TIs and their creation is well beyond the scope of this thesis, the remainder of this chapter will aim to briefly discuss the history of topological insulators and the adaptation to photonic topological insulators (PTIs). . The chapter will also illustrate a few types of common PTIs and then conclude with an outline of the remainder of this thesis.

1.2 A brief history of TIs in condensed matter

Topological insulator materials were first theoretically derived based on replicating the integer quantum Hall effect for physical systems in the field of condensed matter physics around the 1980s [3, 4]. The materials were then experimentally created using compounds comprising of bismuth, selenium, tellurium, and tungsten, among others, and are based on the coupling of the spin and orbital angular momentum of electrons for these heavy metals [5, 6, 7] under external magnetic fields and periodic potentials. The quantum Hall effect states that under an external magnetic field, electrons move in cyclotron orbits that are quantized, creating discrete conductivity states called the Hall conductance. For topological insulators, this quantization was leveraged to created topological propagation as shown in figure 1.2 by the means of a geometric or topological phase.

The topological property under consideration for these materials are not the number of holes as discussed in figure 1.1, but are based on the global topology or curvature of the energy band structure of the material. For periodic or pseudo-periodic materials, the energy band diagram, also known as the dispersion diagram, can be easily calculated and plotted based on the Bloch's theorem for periodic structures. Depending on the curvature of the energy bands, each band is assigned a topological phase (zero or non-zero) and when materials with dissimilar topological phases at the same frequency are placed next to each other, topological transport is observed at

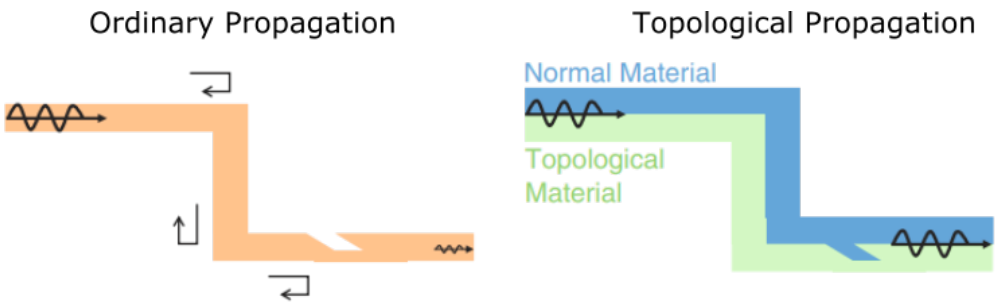

Figure 1.2: As energy propagates on surfaces with bends or defects in the propagation path, some amount of energy is usually reflected backwards or scattered into other directions which reduces device efficiency. Topological propagation overcomes this by creating modes at the interface between materials, that are forced to propagate in only a particular direction. Such scattering immune modes are incredibly robust and are said to be 'topologically protected' (Source: [8]).

the interface between them [9]. These interface or edge modes were found to be highly resistant to impurities in the material [10], fabrication defects and any bends in the propagation path [5]. These results are of great significance as commonly, all these factors contribute to energy scattering which is detrimental to material propagation length and overall device efficiency.

1.3 Topological phases

A mentioned above, the topological property that makes these materials so interesting is based on the curvature of their energy bands. As as wave propagates over the fundamental cell or unit of a periodic or pseudo-periodic structure, it accumulates some phase. If a plane wave is propagating in a straight line, the phase is simply expected to be the product of its wave number and the traveled distance. When propagating in a closed loop path, ordinarily, this value is zero as wave loops back and its starting and ending phases must align. However, in certain conditions, this value can be non-zero and the wave is said to have accumulated some phase due to the geometry of the closed contour. Materials where the wave accumulates zero phase while traveling in closed paths are called trivial and materials where the phase accumulation is non-zero

are called non-trivial. This non-trivial behaviour of geometric phase was observed in classical [11] and quantum mechanical [12] systems is called the Pancharatnam-Berry phase or simply, the Berry phase.

Figure 1.3 shows an excellent example of phase accumulation due to transport on a closed, curved contour [13]. This system of geometric phase accumulation is also seen in helical waveguides [14] and Foucault pendulums [15].

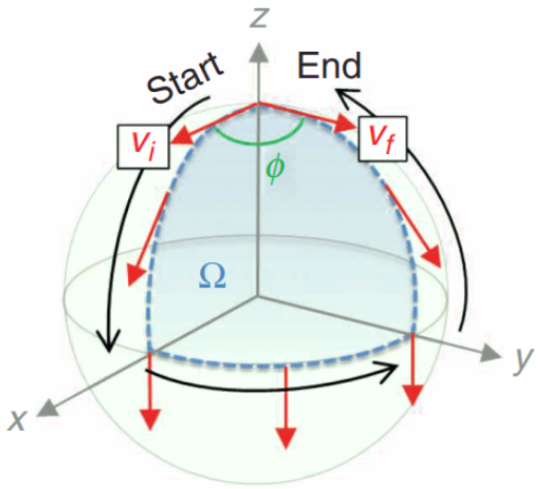

Figure 1.3: As the wave propagates on a spherical surface from the north pole to the equator and back to north pole along a closed, curved contour, it accumulates some phase. The difference between the starting and ending phase is called the geometric phase and is governed by the curvature of the closed contour and the angle subtended at the center of the sphere (Source:[8]).

For periodic or pseudo-periodic systems, the closed contour is defined by the boundaries of the first Brillouin zone.

1.3.1 Berry Phase

To mathematically calculate the Berry phase, the periodic or pseudo-periodic lattice is defined by an eigen value problem in momentum space (also called reciprocal space, inverse space or k-space):

$$H(k) \cdot \Psi_n(k) = \lambda_n(k)\Psi_n(k) \tag{1.1}$$

where $H(k), \Psi_n(k)$ and $\lambda_n(k)$ are the Hamiltonian, eigen wave function and eigen energy of the system, all defined in k-space. The subscript n represents the order or the number of the energy band under consideration.

Once the wave function is solved for, a Berry connection or Berry potential (analogous to a vector magnetic potential) can be calculated as:

$$A_n(k) = i\langle \Psi_n(k) | \nabla_k | \Psi_n(k) \rangle \tag{1.2}$$

where $A_n(k)$ is the Berry connection of the n^{th} band.

Next, the Berry phase for each energy band (ϕ_n) is calculated by integrating the Berry connection over a closed contour in k-space by:

$$\phi_n = \oint_K A_n(k) \mathrm{d}k \tag{1.3}$$

However, much like the vector magnetic potential, the Berry connection is also gauge dependent. A possible method to remove this gauge dependency, as seen in electromagnetics, is to define a new quantity called the Berry curvature (Ω_n). The Berry curvature is defined as the curl of the Berry connection and Stoke's theorem can then be used to alternatively define the Berry phase in terms of the the Berry curvature as well.

$$\Omega_n(k) = \nabla_k \times A_n(k) \tag{1.4}$$

$$\phi_n = \int_S \Omega_n(k) \mathrm{d}^2 k \tag{1.5}$$

The advantage of this alternative way to calculate the Berry phase is that the the Berry curvature is not gauge dependent and surface under integration in k-space can be defined in

standard terms as the limits of the first Brillouin zone: $-\pi/a \leq k_x, k_y \leq +\pi/a$ or $0 \leq k_x, k_y \leq +2\pi/a$ where a is the periodicity of the periodic or pseudo-periodic lattice and k_x and k_y are the unit wave vectors in the plane of wave propagation.

The calculated Berry phase is an invariant quantity and is described as a global parameter of the material. This implies that it is not affected by small changes made to material or how the edge of the material is defined and, much like the Hall conductance, is a quantized quantity.

For periodic and pseudo-periodic electromagnetic systems where the integration area is given by the limits of the first Brillouin zone, the Berry phased is quantized in 2π. Dividing the Berry phase by a factor of 2π gives rise to the topological invariant called the Chern number, which denotes the level of quantization.

When materials with differing Chern numbers or Berry phases are placed next to each other, an interface is created with different topological invariants on both sides (can also be between a trivial and non-trivial material). To bridge the gap between these materials, a topological phase transition occurs [9] which can be thought of as a bridge state at the interface. The interface states span across the bandgap of the materials and are often directional in nature. Because they exist in the bandgap, there are no other states nearby for the energy to scatter or couple into and highly confined guiding occurs. The difference in Chern number or the level of quantization for the two materials determines how many of these interface or edge states exist and each state can be thought of as an independent mode of the waveguide created at the boundary between these materials with dissimilar Chern numbers [16]. Since the Chern number is property of the material bulk and the number of these topological edge modes is solely determined by the bulk property of the material, this phenomenon is known as the bulk-edge correspondence [9].

1.4 Chern Numbers: creation and variations

While subtle differences exist between electrons, phonons, and photons (the first is a fermion while the latter two are bosons), when interacting with materials arranged in a lattice, there are similarities in the way these three waves behave. This has allowed for an easy transition from electronic topological insulators to acoustic and photonic topological insulators (PTIs). Molecule lattices in electronic systems are replicated through printed metal and dielectric metasurfaces and analyzed based on the construction of the energy band diagram given by Bloch's theorem for periodic structures through the Brillouin zones at acoustic, microwave and optical frequencies.

When the Chern number is calculated for any arbitrary band of a structure, the value obtained after integration is usually zero. However, due to the introduction of an external magnetic field, the time reversal symmetry is broken and the material becomes non-reciprocal [9]. This non-reciprocity leads to a non-trivial Chern number and lends directionality to the created interface states. Such materials, with a broken time reversal symmetry, are commonly called Chern insulators or Chern PTIs. The direction of the external magnetic field decides the direction of wave propagation [17].

It is also possible to generate non-trivial Chern numbers while maintaining the time reversal symmetry by breaking the spatial inversion symmetry of the structure instead. Since the addition of an external magnetic field and the use of gyrotropic media is not always feasible, PTIs with broken spatial inversion symmetry pose an attractive alternative.

To allow for a phase transition and the creation of bridge modes at the interface as discussed in the previous section, a degeneracy or point of intersection between two or more energy modes must exist. The breaking of either the time reversal or spatial inversion symmetry breaks open this degeneracy, creating a band gap. Creating a bandgap by breaking the time reversal symmetry ensures a non-zero Chern number and interface or edge states pop up in the bandgap when this material is interfaced with another material that is trivial (Chern number=0)

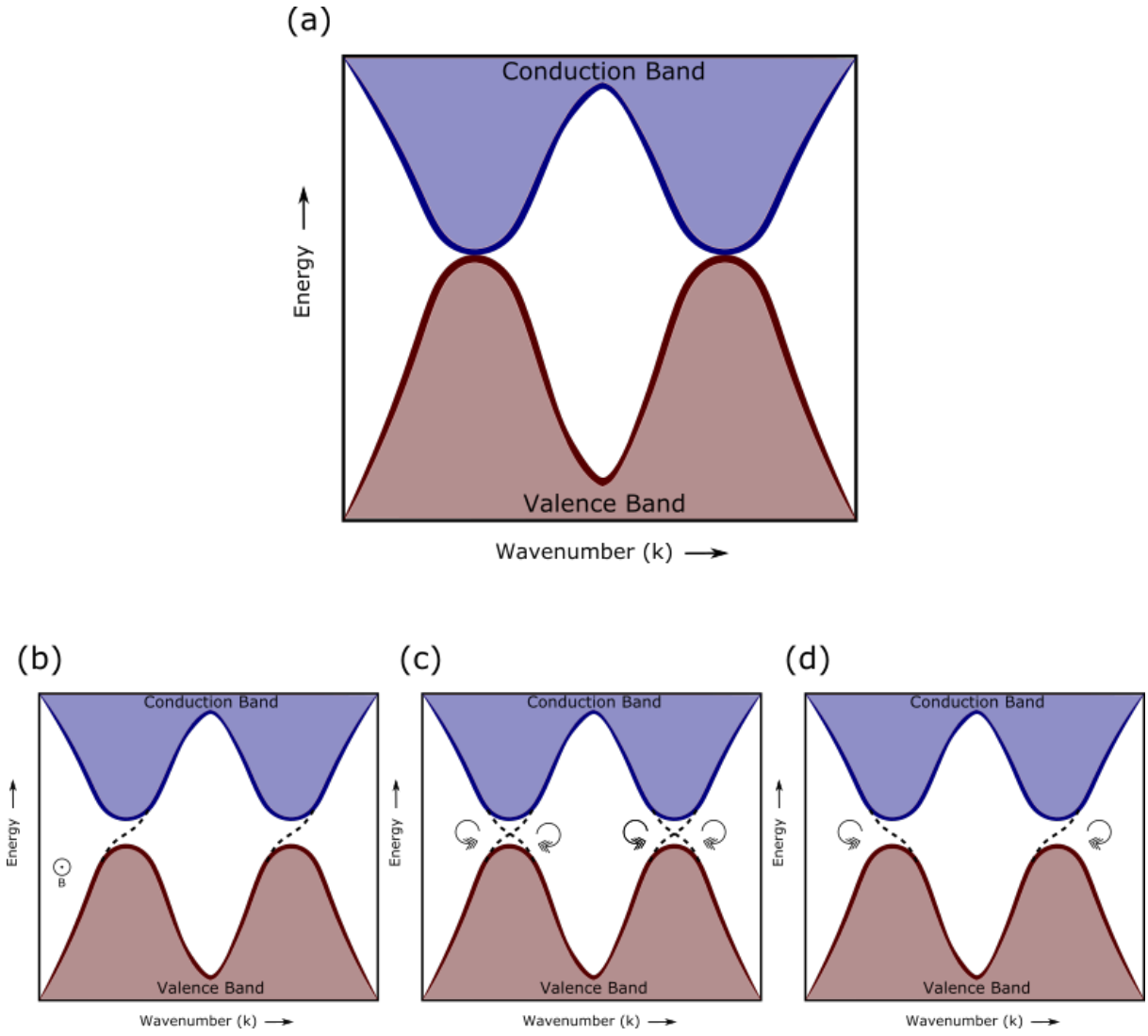

Figure 1.4: (a) Energy band diagram showing degeneracy points between the conduction and valence bands. For metasurfaces, the conduction and valence bands can refer to any dispersion bands with opposite group velocities. (b) Chern PTIs can be created by breaking the time reversal symmetry using an external magnetic field. Unidirectional interface modes are created in the bandgap and the direction can be reversed by reversing the applied magnetic field. (c) Spin Chern PTIs are created by breaking the spatial inversion symmetry leading to an opening of the bandgap at a multi-band degeneracy (at least four modes at each degeneracy point). This causes two interface modes with opposite hybrid polarizations in each half of the Brillouin zone. (d) Valley Chern PTIs are also reciprocal devices with a broken spatial inversion symmetry. Only two bands intersect at each degeneracy and each half of the Brillouin zone supports an interface mode with an opposite sense of rotation.

or a material with a different non-zero Chern number. Breaking the inversion symmetry does not generate a non-zero Chern number but a few clever mathematical tricks can be use used to defined special variations of the Chern number that also have similar robustness and directional properties. The two most common among these are the spin Chern number and the valley Chern number which are based on the spin and valley quantum Hall effects, respectively. Figure 1.4 shows the difference in the interface modes created for each type of PTI.

1.4.1 Spin Chern PTIs

Spin Chern PTIs are based on structures that show a double degeneracy in their band structure, i.e.- at the point of degeneracy, there are four bands that intersect that the same energy level. Breaking the inversion symmetry of this structure allows for the opening of the bandgap. The lower two band and the upper two bands move together and create a hybrid mode in the region of their overlap. The mode hybridization can create circularly polarized (CP) modes: by overlapping the two lower modes which are transverse electric and transverse magnetic or horizontal and vertical, a hybrid CP mode can be obtained. Since this system is reciprocal, the same hybridization, but flipped, happens on the opposite side of the Brillouin zone and an interface mode bridging the bandgap across the Brillouin zone is created [18] as seen in figure 1.4(c). Each polarization is assigned its own value of Chern number called the spin Chern number and it is opposite for both hybrid modes. Bi-anisotropic coupling or changing the symmetry of the internal features of the unit cell provides an easy method to break the inversion symmetry for this class of PTIs [18, 19, 20].

These modes show directionality based on the polarization of the hybrid mode and are sometimes called spin-momentum locked modes where the spin is given by the wave polarization and the momentum is defined as the direction of wave propagation. Exciting one polarization will lead to a mode that propagates in a particular direction and exciting the second hybrid polarization will cause the mode to propagate in the opposite direction. This spin-momentum locking is very

robust and as long as structural defects, sharp bends in propagation paths, obstacles, or other imperfections do not convert one polarization to the other, Chern insulator like robust transport is observed.

1.4.2 Valley Chern PTIs

Another common type of PTI based on breaking of the spatial inversion symmetry is the valley Chern PTI. As mentioned previously, in systems with time reversal symmetry, the integration of the Berry curvature over the first Brillouin zone provides a Berry phase of zero. However, if integrated over only *half* of this area, a non-zero Chern number can be obtained. If the Brillouin zone is divided into two halves, the each half will result in a non-zero Chern number that is equal in magnitude but opposite in sign, resulting in a net zero Chern number when added. If a device is design with enough care that a wave propagates only in the direction governed by the left or the right side of the Brillouin zone, it can be used as a non-trivial PTI [21].

Similar to other types of PTIs, the system must contain a degeneracy point in the energy band diagram that is opened by breaking the spatial inversion symmetry. Symmetry point groups can be exploited to find designs that show the required degeneracies [22]. Once the gap is opened and two materials with opposite spin Chern numbers are interfaced, an interface state emerges in both halves of the Brillouin zone as seen in figure 1.4(d). Both the interface states usually have an orthogonal sense of rotation which implies that an incoming wave will pick its propagation direction based on which half of the Brillouin zone matches its polarization.

Many research works published in recent years can be found that show detailed, step-by-step tutorials on how to calculate and differentiate between the different Chern numbers with well defined examples in each category [9, 8, 23, 24].

1.5 Scope of the thesis

This thesis will primarily focus not the development or classification of PTIs as discussed in this chapter, but on the usage and applications of photonic and microwave topological insulators as waveguides and radiators.

Chapter two explores an alternative type of interface mode for finite height, dielectric photonic crystals based on transverse resonance and another type of topological phase called the Zak phase. The transverse resonance method is based on energy trapping at the surface of a photonic crystal (PhC) due to variable truncation or *cell sliding* and results in rotational eigenmodes that show great confinement. The Zak phase, on the other hand, is a special case of the Berry phase and introduces a degree of topological protection to the interface mode created by the same PhC used for the transverse resonance method but by *cell scaling* instead. Simulation results are discussed for both cases with fabricated device results for the Zak phase structure.

Chapters three and four use a previously tested and fabricated spin PTI design and analyze the effect of the light line and mode cut-offs introduced by finite height metallic metasurface PTIs. Chapter three nudges the existing boundary of PTI wave guiding applications by exploring aperture antennas. It examines the problems of abrupt truncation of a PTI waveguide to free space and its potential effectiveness as an antenna at this truncation edge. It also provides a brief but through and comparative study of device performance and physical dimensions as compared to the simple and conventional aperture antennas, that are in use today.

Chapter four explores the usage of the spin PTI metasurface above the light line to create a leaky wave antenna. It showcases an interesting ability of the leaky PTI modes propagating in closed loop paths to generate beams with variable orbital angular momentum (OAM) charges that are characterized by a vortex phase progression and an intensity null along the beam axis. Simulation data shows the ability to create beams with arbitrary OAM invariants based on physical and electrical path lengths and possible methods for beam multiplexing. A sample device shows

measured data that reflects this vortex beam generation.

Finally, chapter five concludes with a summary of the thesis along with a brief note on possible future applications and interesting developments in the field of photonic topological insulators.

Chapter 2

Interface Modes based on Transverse Resonance and Zak Phase

2.1 Introduction

In condensed matter, a spin-momentum locked wave indicates that an electron with a defined spin can travel only in one direction while an electron with the orthogonal spin can travel only in the opposite direction, i.e., the spin and propagation direction (momentum) of the electron are strongly coupled. In microwave and photonics, the spin and momentum of an electron are analogous to the polarization and propagation direction of the electromagnetic wave or photon. So for certain types of microwave and photonic topological insulators (PTIs), the sense of wave polarization (clockwise/anti-clockwise) determines the direction in which the wave can travel, leading to reflection-free and polarization dependent beam propagation. This incredible robustness has many important ramifications in the field of energy guiding, among which is a lossless and full duplex communication at both microwave and optical frequencies [25] using PTI devices that support these highly confined interface modes.

The creation of interface modes with some degree of this type of spin-filtering or unidirec-

tional robustness is essential as it can eliminate the need to carefully tailor a turning radius for waveguides. This, in turn, can greatly reduce device area, leading to applications in miniaturization. Waveguides made with topological materials can be designed with acute, obtuse or miter bends without fear of scattering and reflection along with higher tolerances in geometry defects due to fabrication limitations.

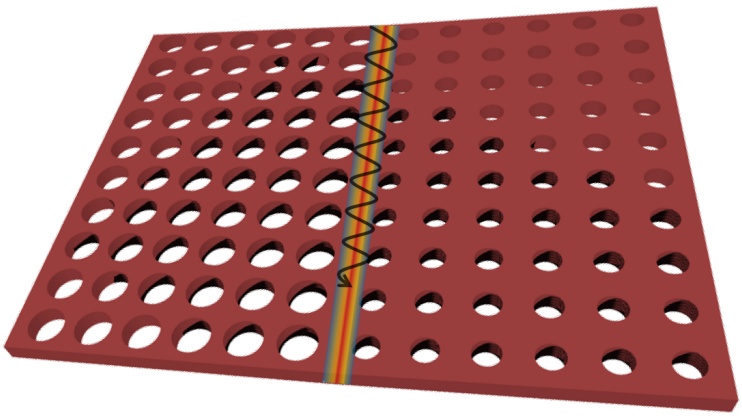

Figure 2.1: Schematic of a finite height dielectric structure supporting an interface mode between two photonic crystals with the same C_{4v} symmetry on both sides of the interface

This chapter demonstrates and analyzes the creation of interface modes with differing forms of spin-momentum locking in practical, finite height, all-dielectric structures. The first structure, which possesses a more restricted class of spin-momentum locking, involves an analysis of the reflection phase at the material truncation edge. The second structure, which displays interface modes with behavior more typical of PTI spin-momentum locked modes, are based on a one-dimensional Zak phase analysis. The designs use a simple fabrication geometry involving the same cubic unit cell with a C_{4v} symmetry on both sides of the interface as shown in figure 2.1. The subsequent sections detail the theory, existing designs, and necessary conditions to create an interface mode using both approaches. The proposed device designs, demonstrated via simulation and experimental data for a Zak phase structure in the magic-T configuration (four way junction in unidirectional structures), depict its intrinsic spin-momentum locking capabilities

and are provided as examples.

2.2 Interface modes through transverse resonance

One theory for the existence of confined interface modes is based on reflection phases [26, 27, 28]. When a wave is incident on a material at a frequency within its bandgap, all energy must be reflected. The phase of the reflected wave is analyzed and if two materials reflect energy with the opposite phase, then the 'nature' of their respective bandgaps must be opposite. If material 1 reflects a wave with phase '$+\chi$' and we assume this bandgap has a large inductive impedance, then if the phase reflecting off of material 2 is '$-\psi$', then the bandgap for material 2 has a large capacitive impedance based on their opposite signs. In general, an incoming impinging wave will see a $+jX_1$ impedance for material 1 and a $-jX_2$ impedance for material 2. If the absolute value of these reactive impedances is the same ($|X_1| = |X_2|$), a transverse resonance along the boundary between materials 1 and 2 is established. The wave is reflected at a grazing angle to both materials and propagates along their interface, creating a new edge or interface mode. Figure 2.2 shows an example of the wave hitting the finite height dielectric PhC from the direction of the interface and the measured phases of the reflected wave for a shifted and un-shifted sample. The waves in the two cases are $\sim 180^\circ$ out of phase with each other, showing transverse resonance. While this may be a necessary condition for the existence of such a 1-D interface mode, it is not a sufficient condition for spin-momentum locking. Spin-momentum locking can be achieved in a few ways: the presence of a topologically non-trivial bandgap, the use of unit cells where the eigenstates or field profiles are rotational in nature, or via an evanescent coupling with the appropriate source excitation [29, 30, 31]. The first method of non-trivial bandgaps creates highly robust modes due to an intrinsic spin-momentum locking enforced by symmetry, while the others create interface modes with a reduced robustness in spin-momentum locking that may exist only for certain propagation directions and is more susceptible to scattering

at sharp corners and defects.

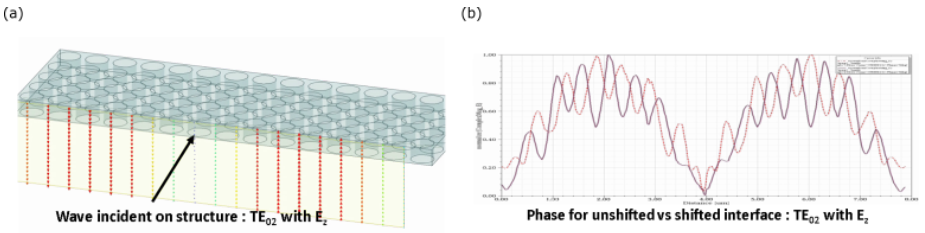

Figure 2.2: (a) Schematic of a wave incident on a finite height dielectric PhC. (b) Phase of the wave reflected off of a shifted and un-shifted sample at a frequency within its bandgap. The reflected waves are 180° out of phase, showing transverse resonance.

The transverse resonance method leads to interface modes that are more susceptible to scattering and coupling into the surrounding bulk modes upon encountering defects or discontinuities. This is due to the fact that the interface mode is based solely on reflection phase; its unidirectionality is the result of the rotational nature of the fields that are created by the intrinsic features of the unit cell. For example, the cylindrical air hole in the proposed unit cell design forces the fields to circulate around it, creating a rotational eigen field. A similar effect can be obtained by creating features that represent other regular or irregular polygons- with a few exceptions based on symmetry conditions [32]. On the other hand, non-trivial bandgaps can lend topological protection to the created interface modes which, based on wave polarization, makes them immune to a wide class of scattering. This immunity can either exist everywhere in the plane of propagation, as in standard PTIs, or only along certain specific directions, as detailed in the latter half of this chapter.

2.2.1 Structure: pseudo-finite vs finite height

Our proposed design draws inspiration from a simple structure comprised of infinite dielectric cylinders arranged in a square lattice that has been previously demonstrated [33]. Since no structural variation is observed along the vertical height or in the bulk of the material along the direction of propagation, the only variation that a wave encounters is at the interface change that

is lateral to the direction of wave propagation. This implies that a 1-D line integration of the Berry connection will suffice to find the Berry phase of the structure, along a particular direction. This reduced dimensional computation of the Berry phase is called the Zak phase. However, while providing detailed insight into the conditions for the existence of an interface mode, the infinite dielectric height condition is realized by sandwiching a structure of finite height between two large PEC sheets [26, 34]. This allows for easy isolation of modes and these previously proposed pseudo-finite height structures support only a TM bandgap and the confining metallic sheets allow for easy excitation of only the desired TM mode while suppressing all TE modes that could interfere with the desired edge mode.

To loosen the restrictions that the PEC confinement places on the design, the behavior of a fully finite structures is analyzed, along with its potential for practical applications. However, with a finite height that is comparable to the unit cell dimension, the band structure changes for both TE and TM modes, pushing all bands closer together. The bandgaps are much narrower due to this mode compression, which causes an increased difficulty in the excitation of a pure TE or TM mode. Therefore the presented approach for finite height dielectric slabs must based on calculating the entire band structure without polarization-based mode segregation. To ensure that the resultant mode is guided and not radiative or cut-off, the location of the modes with respect to the light line is also an important consideration.

2.3 Interface modes through cell-sliding

Since the photonic crystal structure is periodic and infinite, a slide or a shift of the internal features of a single unit cell is only noticeable at the edge. This is considered a variable edge truncation of the photonic crystal as the only means to distinguish between the original and the slid PhCs is at an edge. Based on this sliding of internal features, a previously proposed, pseudo-finite height design interfaces a PhC with a shifted version of itself and an edge mode

is obtained at the '*hole/half hole*' interface [33]. While originally described as existing due a gauge variation property of the Zak phase that will be shortly discussed, this work aims to justify these interface modes by an alternative theory of arbitrary edge truncation or cell sliding and the trapping of energy states by PhCs in their bandgap. The schematic of the finite height implementation of this case is depicted in figure 2.3(a).

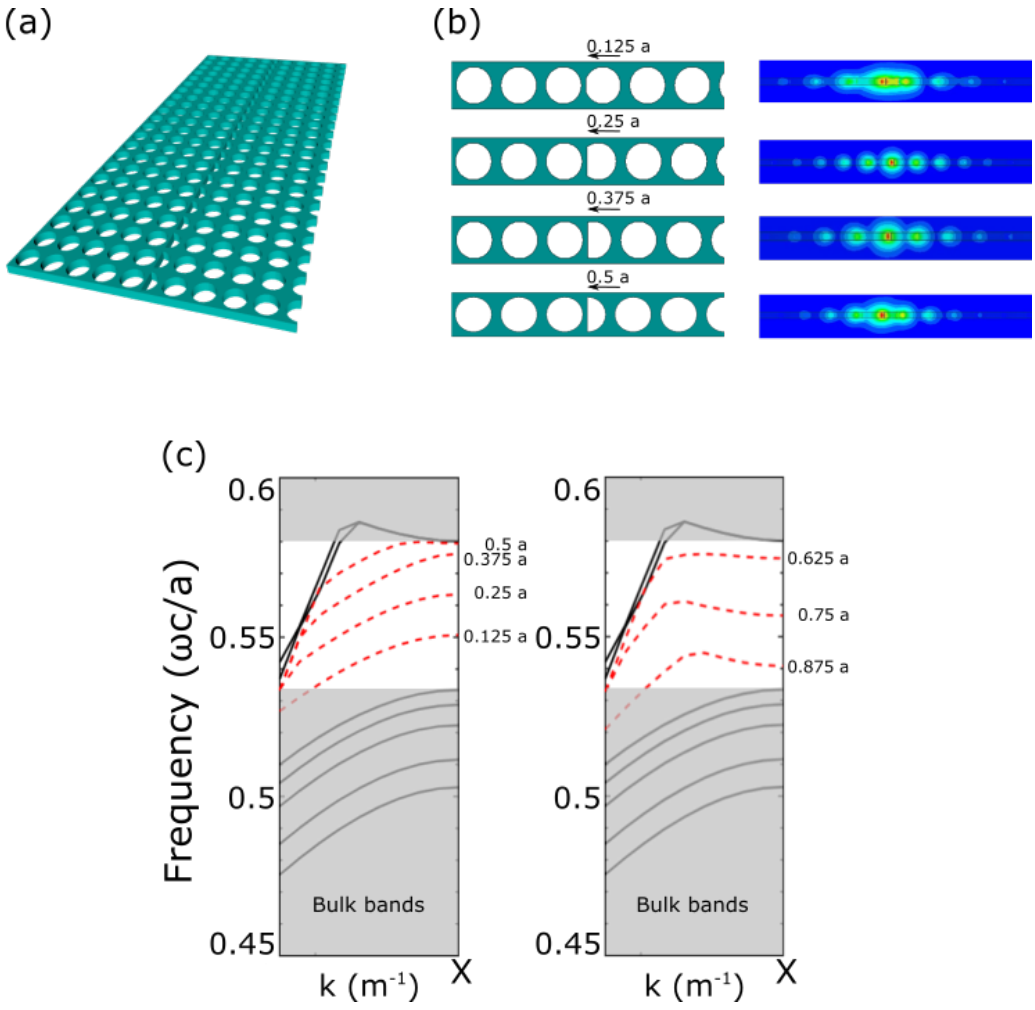

Figure 2.3: (a) Device schematic of a cell sliding interface. The material on the right is shifted by half a unit cell period. (b) Top view (left) depicting various values of cell sliding across the interface and front view (right) showing the corresponding field localization where a is the cell periodicity. (c) Energy bands around the high symmetry X point of the first Brillouin zone. The bulk bands are in black and the interface modes that span the un-shaded bandgap for different cell sliding values are in red

Figure 2.3(b) provides a graphical top view of how the original and shifted PhCs are interfaced for different sliding values as well as a front view of the full wave simulation that shows the existence of an interface mode for the corresponding sliding values. The maximum energy is seen at the center where the original and shifted PhCs form an interface, with varying degrees of confinement. Leakage into the sides is forbidden due to the fact that these interface modes exist within the PhC bandgap. Figure 2.3(c) shows the movement of the interface mode through the dispersion diagram around the X point of the first Brillouin zone of a square lattice. Rigorous eigenmode and driven full wave simulations were performed to verify the emergence of the interface mode into the bandgap region of the PhC from within the lower bulk modes. As the sliding increases and the center of the air hole moves closer to the interface boundary, the mode moves up towards the top edge of the bandgap until a shift of exactly half a period has been achieved. Subsequently, a descent back down into the bulk modes with an opposite group velocity is observed till the sliding value is equal to a unit cell period and the interface between the materials is indistinguishable. The change in group velocity simply represents a change in the direction of rotation of the eigenfields at the interface.

Further investigations show that this phenomenon is closely linked to the surface modes that occur at the variable truncation of photonic crystals [35]. This phenomena details the trapping of energy at the surface of a PhC within its bandgap due to the destruction of translational symmetry that occurs due to the variable truncation. Replacing the air medium above this variably truncated PhC with a pure bandgap material, like the un-truncated or un-shifted version of the original PhC, results is higher mode confinement by further reducing evanescent decay in vacuum. However, at the frequency where a transverse resonance is established at the boundary between the ordinary and variable truncation PhC, the longest propagation lengths are observed, thereby creating a 1-D interface mode with the greatest confinement and least loss.

Transverse resonance is established when the phase difference between waves reflected off of both PhCs is 180°. A minimal drop in performance is observed when the phase difference

between the shifted and un-shifted PhCs lies in the range of 140° to 200°. Figure 2.4 shows the frequency at which transverse resonance is established for varying shift or truncation values and they follow a similar trend to that observed in figure 2.3(c).

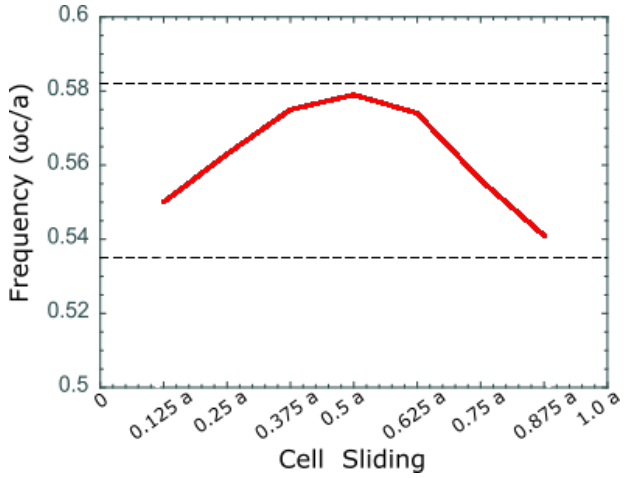

Figure 2.4: Normalised frequencies of the transverse resonance for a range of cell sliding values. The difference between the reflection phases of the two PhCs is 180° at this frequency.

It is important to note that since the reflection angle (in the case of transverse resonance) is being calculated transverse to the direction of propagation (top view in figure 2.3(a)), only shifts in the transverse direction result in edge modes. A shift of the air hole only along the propagation direction (in-plane vertical) results in no interface mode emergence in the band gap. Diagonal sliding, which is equivalent to a lateral slide *along* with vertical movement, results in the emergence of interface modes as discussed above for purely lateral sliding as seen in figure 2.5 .

Since the eigen fields of the structure are rotational in nature, with correct alignment, it results in spin-momentum locking and the structures can be unidirectionally excited using a circularly polarized source with an in-plane rotation. However, the robustness of such interface modes is very weak and standing waves are established when the interface modes encounter sharp turns that destroy the alignment. The scattered and reflected energy easily couples into the bulk modes that are outside the bandgap and the efficiency of the structure as a means to guide

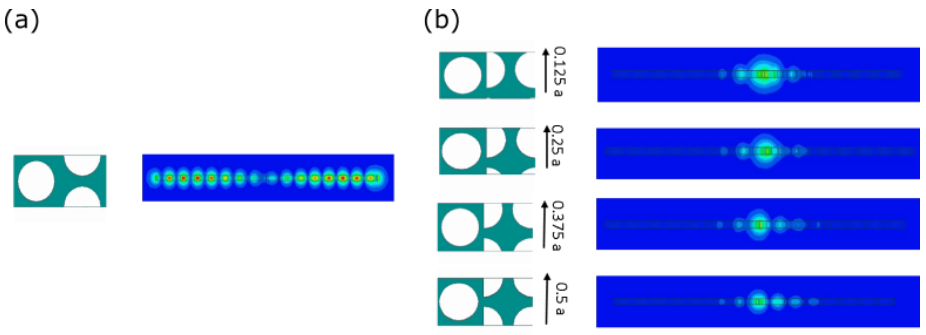

Figure 2.5: (a) Lack of interface modes with a vertical shift. (b) Interface modes with a diagonal shift are similar to those created by a lateral shift. No interface modes are created with a vertical shift as the wave is incident transverse to the interface direction and any sliding along the propagation direction does not affect the reflected wave.

waves in a highly confined manner is greatly reduced. This low robustness indicates defect-mode like behaviour as seen in conventional PhC waveguides along with the absence of a nonzero topological invariant for each sliding value. The existence of this type of an interface mode is dependent on factors beyond topology, namely trapped two-dimensional PhC surface states caused by the breaking of translational symmetry, and these modes are further confined and strengthened by transverse resonance.

2.4 Topological Invariants and the Zak phase

As discussed in the previous chapter, most PTI designs are made up of repeating periodic or pseudo-periodic unit cells and are based on the opening of a non-trivial bandgap [21, 20, 19, 36] in their band structure. The bandgap is then characterized based on the Berry curvature of the bands that exist beneath it and is assigned a topological invariant based on a calculated Berry phase.

Most common implementations of topological devices are based on confining the guided mode in the horizontal plane, leading to a surface integral of the two dimensional eigenstates in the first Brillouin zone that covers all possible propagation directions to calculate the geometric

phase. The topological invariant thus obtained is called the Chern number. Similarly, when analyzed in only one dimension, a line integration of the Berry connection is performed [37, 38] and the calculated topological phase is referred to as the Zak phase and *does not have an invariant associated with it* [39, 40]. While the Berry phase for Chern and spin Chern insulators exists in integer multiples of 2π, the Zak phase can take only two values of 0 and π [41, 39]. This is because of a difference in normalization coefficients. Since the geometric phase obtained when a 2D integration is performed over a curved surface (such as a mode in the dispersion diagram) is dependent on the angle subtended by the surface at the center of an imaginary sphere, the normalization co-efficient includes a π term. For a linear integration, as required for the calculation of the Zak phase, there is no such subtended angle and the normalization term is a purely rational number. When two materials with differing topological phases share a boundary, a new mode that is robust and spin-momentum locked is created at the interface between them.

While the mathematical form of the Berry phase is presented in chapter 1, from an electromagnetic perspective, the eigenstates of the Hamiltonian simply refer to the electric or magnetic fields of the eigenmodes of a unit cell for a periodic structure. Assuming G_n are the fields (electric or magnetic) of the n^{th} mode of a periodic structure in inverse or k-space, a simplified equation to calculate the Zak phase $\mathbb{Z}^n$ of the n^{th} band is given by:

$$\mathbb{Z}^n = i \oint_{BZ} \langle G_n(k) | \nabla_k G_n(k) \rangle dk \tag{2.1}$$

$$\approx Im \left\{ \ln \left(\prod_{0}^{K-1} \langle G_n(k_i) | G_n(k_{i+1}) \rangle \right) \right\} \tag{2.2}$$

where K represents all possible values of the wave number in the first Brillouin zone along the chosen dimension (usually k_x or k_y and is in-plane transverse to the direction of propagation).

This line integration examines the rotation undergone by the eigenfields (E/H field) as we traverse the first Brillouin zone. If the field profiles at the start and end match exactly, a Zak phase

of zero is obtained, while if the field profiles undergo sufficient rotation to have accumulated phase, the Zak phase of the energy band is π. To further simplify the integration, for transverse magnetic (TM) and transverse electric (TE) modes, one can selectively switch between the vertical (majority) components of the E and H fields, respectively. The minor components of the E/H fields do not contribute significantly to the overall integration and can be neglected for ease of calculation. However, for complete accuracy and to obtain an exact value of 0 or π for each band, a full summation of the fields along all axes must be performed. It is important to note that the Zak phase, unlike the Chern number, is not a gauge invariant quantity. It is a gauge dependent value and is tied to the choice of center point in the Brillouin zone of the unit cell under consideration[39, 40]. If the high symmetry point of Γ is considered the start of the first Brillouin zone and the calculated Zak phase is 0, then shifting the start of the first Brillouin zone to the X point will result in a Zak phase of π.

The most common technique used to achieve reduced dimensionality is the use of infinite height structures to remove any structural variation or mode cut-offs caused by a finite height along the vertical axis. For practical purposes however, as used for the structures mentioned in subsection 2.2.1, finite height structures sandwiched between perfect electric conductor (PEC) or perfect magnetic conductor (PMC) sheets are used. These top and bottom sheets limit the propagating modes to either solely TM or TE modes, respectively, and emulate infinite height. This pseudo-finite height also ensures that the band structure remains largely undisturbed with respect to the material thickness between the bounding sheets and that the location of the modes with respect to the light cone and possible radiation leakage are unimportant. However, the bounding metallic sheets or artificial magnetic structures pose various difficulties when measuring near field confinement, transition to and from conventional feeding structures and for deployment in real-world applications.

Figure 2.6 shows an example of a dielectric unit cell of finite height with an air hole in the center and it's dispersion curve. Assuming the first mode is a TM mode, the majority field

component is E_z, and the wave is propagating along the y-axis, the Zak phase of this TM band can be calculated by:

$$\mathbb{Z} = i \oint_{k_x} E_z(k_x)^* E_z(k_{x+1}) dk_x \tag{2.3}$$

where k_x spans the high symmetry points of $-X$ to Γ to X for the first Brillouin zone of a square lattice. This equation provides the angle accumulated by the z component of the E field for the first TM band along the k_x direction.

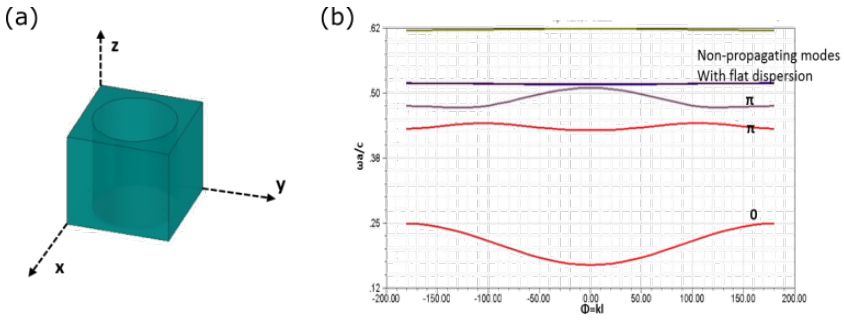

Figure 2.6: (a) Schematic of a finite height cubic dielectric block with an air hole (b) Dispersion diagram showing the normalized frequency vs phase dispersion. The wave is assumed to be propagating along the y axis and the integration is therefore performed along k_x

2.4.1 Interface modes with cell scaling

Analysis of the energy band diagram for the chosen C_{4v}-symmetric unit cell reveals the presence of many higher order bandgaps and select gaps possess an opposite reflection phase to that of the lowest order band gap [32], allowing for an edge mode if properly interfaced. In figure 2.7(a), the energy band diagram for a cubic unit cell made of silicon with a cylindrical hole in the center is shown with the labeled values of the Zak phase for each band. Bandgaps with opposite topological charge are observed between the second and third bands and fifth and sixth bands. A possible method to interface the two bandgaps occurring at dissimilar frequencies of the same band structure is to reduce the size of the air hole in the dielectric cube [35] as seen in

figure 2.7(b). This results in an increased amount of dielectric in the same unit cell volume which causes the entire band structure to squeeze together and move downwards in frequency.

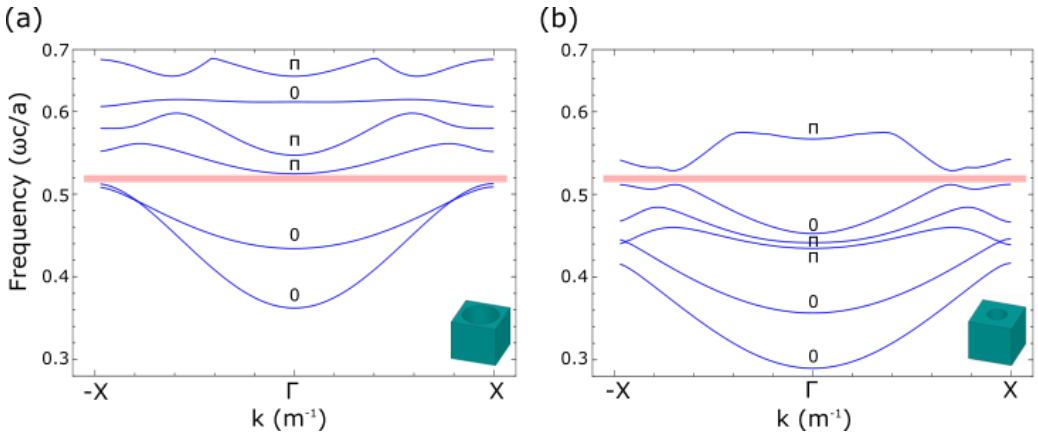

Figure 2.7: (a) Energy band diagram of the original cubic unit cell (b) Energy band diagram of the scaled cubic unit cell. The scaling factor of the air hole diameter is 0.56, while all other dimensions of the dielectric unit cell remain unchanged. The first six bands are plotted and their corresponding Zak phase labeled

While the shapes of individual bands change and the width of the bandgaps decrease, the nature of the bands and the gaps remains unchanged [22] and can be verified by re-calculating the Zak phases for each mode of the scaled design. This simple scaling method enables the interfacing of two different bandgaps of the same structure that exist at different frequencies. Figure 2.7 depicts a side-by-side comparison of the band structure for the original and scaled unit cell. Interfacing the two metasurfaces results in a topologically protected edge mode at the normalized overlap frequency. While scaling the unit cell in all three dimension would have maintained band structure and provided a wider frequency range for bandgap overlap, only the air hole diameter was scaled for easier fabrication and visual clarity. This maintains the same unit cell periodicity, symmetry, and dielectric height across the entire device surface.

2.4.2 Device parameters and measurements

All simulations for the cell sliding and cell scaling methods were initially performed with ordinary silicon as the dielectric (relative permittivity=11.9) for operation at 410 THz (red light) as shown in figure 2.8(a). Unit cell dimensions were chosen to accommodate the fabrication limitations of E-beam lithography techniques with unit cell length and width of 200 nm, dielectric thickness of 200 nm and air holes with diameters of 160 nm. The smaller air holes for the scaled cells were 90 nm in diameter. Figure 2.8(b) shows simulation results for the interface arranged in a straight line, with a miter bend and in a magic-T configuration. The decrease in propagation length is due to the transverse leakage occurring on the side with the smaller holes due to a narrower bandgap width as compared to the side with the larger holes.

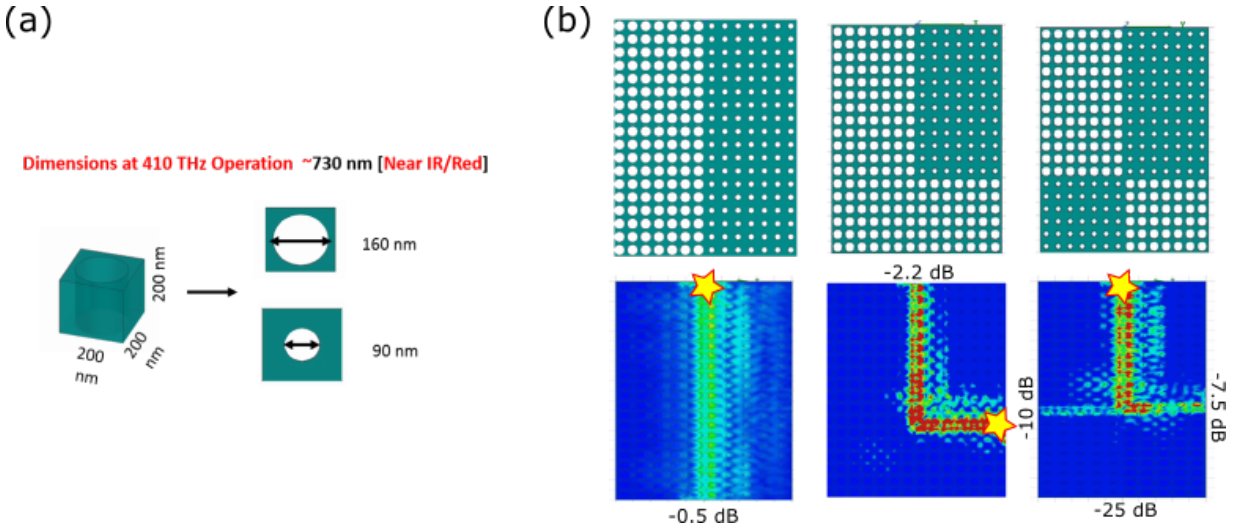

Figure 2.8: (a) Dimensions of the simulated unit cell for the large and small holes (b) Simulation results for an interface mode propagating along a straight line, a right-angled bend and a magic-T configuration. The star represents the location of the source and the value of the output power, assuming a 0 dB input, is printed at the output terminals.

For proof of concept, the design was scaled up in size and slightly adjusted for a dielectric of relative permittivity of 10.2 (Rogers 6010.6), dielectric thickness of 5mm and an operating frequency of 18 GHz. The structure was excited with a simple electric dipole probe and set under a near field scanner to observe energy propagation over the surface.

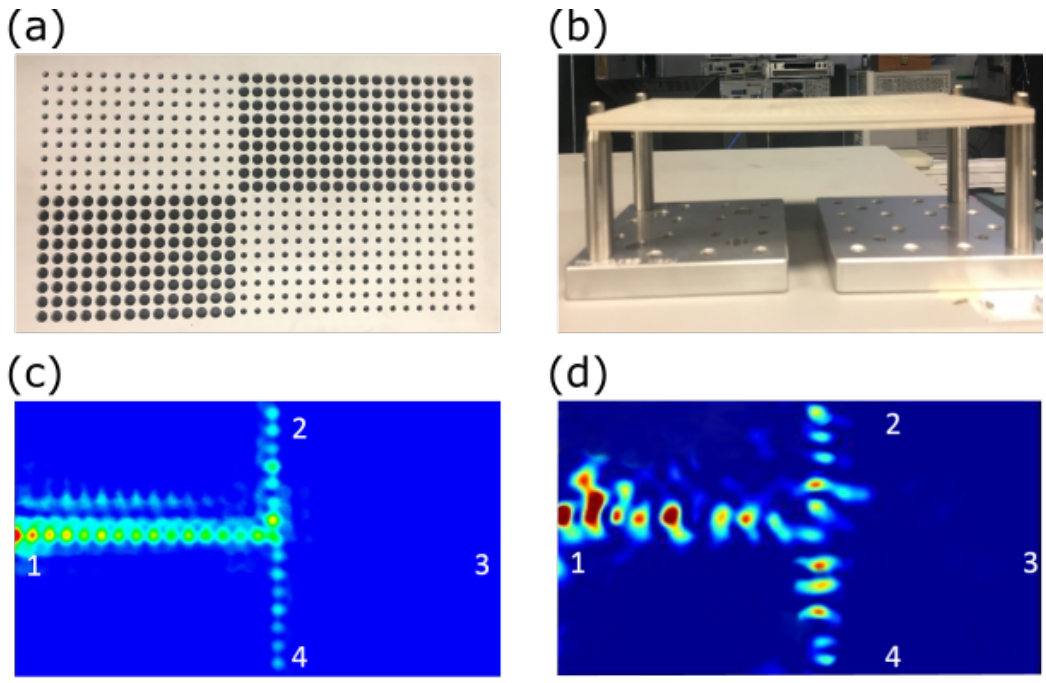

Figure 2.9: (a) Top and side view of the fabricated magic T structure at 18 GHz. (c) Electric field simulation and (d) measurement results of energy propagation in the four port magic-T structure displaying the spin-momentum locked nature of the interface mode. Heavier leakage can be seen in the simulation and measurements towards the side with smaller holes due to the existence of narrow and incomplete bandgaps

Figures 2.9 (a) and (b) show the fabricated structure with a finite dielectric height of 5 mm and figures 2.9 (c) and (d) depict the simulation and measurement results obtained when exciting the device that is patterned in the shape of a four port magic-T network. This PTI magic-T is a special structure designed to test for spin-momentum locking in non-trivial waveguides [42]. Similar to the magic-T network in microwave waveguides, such a system permits energy flow from one entry port into two orthogonal output ports, but forbids it in the third remaining port as a result of the underlying spin-momentum locking. Isolation at port 3 (S_{13}) is -27 dB while S_{12} and S_{14} are -8 dB and -10 dB, respectively. The high isolation is a good indicator of the strongly spin-momentum locked property of the interface modes while the increased leakage into the bulk of the small-hole surface is due to the presence of a narrower bandgap. A narrower bandgap implies closer proximity and easier coupling to the bulk modes, leaking to increased leakage.

The energy leakage around port 1 is caused due to the mode mismatch between the source excitation and the interface mode and can be mitigated by using carefully designed, alternate feeding methods [43, 44].

It is important to note that the energy band diagrams are three dimensional contours that represent all possible energy values of a wave propagating along a given direction in k-space. However, the Zak phase structures are based on a line integration performed along a single fixed direction and the *bandgaps observed exist along those specific propagation directions only*. As is characteristic of most C_{4v} symmetric structures, it is likely that the bandgap closes when propagation occurs along other directions, which results in most Zak phase structures having incomplete-band gaps [26] and possible energy leakage. A wave propagating in the direction where a bandgap exists may see a high degree of confinement at the interface but will see poorer confinement and be more prone to scattering if propagating in a direction where the bandgap narrows or closes. Such structures cannot support propagation paths that curve or bend in arbitrary directions that are characteristic of other PTIs based on a 2D surface integration of the Berry connection, but highly confined topological waveguiding does occur in the directions where the band gap is open and the interface mode lies below the light line. Given the narrower width of the higher order band gaps, there is less isolation between the interface mode and the bulk modes resulting in easier coupling of stray energy into these bulk modes, especially around bends and perturbations. However, for the demonstrated design, this leakage is minimal, does not extend beyond two to three unit cell widths, and is more prominent on the side of the smaller holes where the interface mode exists in the narrower gap as seen in figure 2.9. The chosen periodic structure allows confined and reflection free propagation at all right-angled corners based on its band structure.

Figure 2.10 shows another example of a fabricated structure with a closed loop interface with right angled corners. The measurement results show almost no loss in magnitude as the wave propagates at right angled edges which represent the direction of the open band gap. The leakage

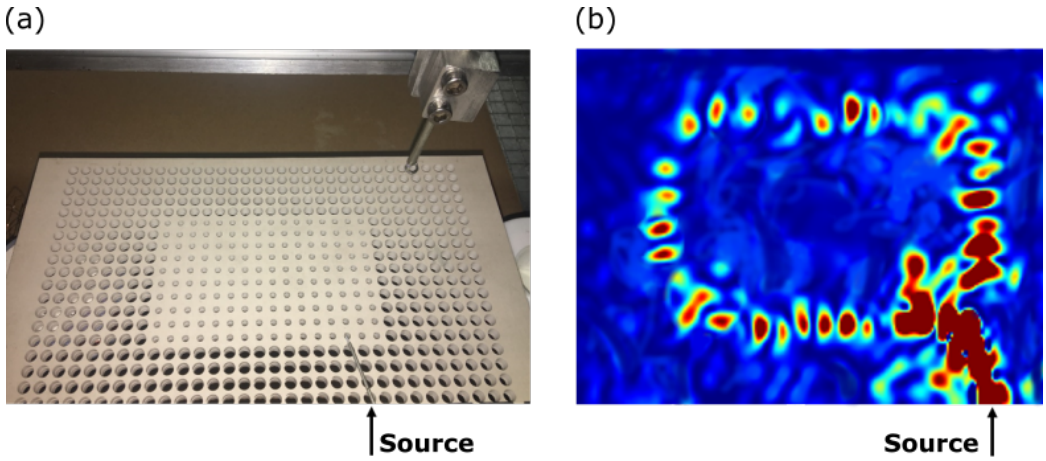

Figure 2.10: (a) Top view of the fabricated surface arranged in a closed square loop with the source and receive probe (b) Measurement results showing the magnitude of the E field as it propagates around the path

seen at the bottom of the image marks the location of the source. The source probe was angled at $\sim 45^{\circ}$ to the interface. This allows for an excitation of an E field component in two directions: transverse and along the interface direction. The two components interact and successfully couple into the rotational eigen mode of this large hole- small hole interface. The created interface mode has a bandwidth of $\sim 2.5\%$

2.5 Conclusions

This chapter focuses on finite height dielectric structures and creating interface modes supported in these structures based on two approaches: transverse resonance or cell sliding and Zak phase or cell scaling. The design utilizes a simple cubic unit cell with C_{4v} symmetry and incomplete bandgap as opposed to the C_{6v} or C_{3v} symmetry cells seen in most Chern number based PTI implementations and aims to utilize multiple bandgaps of the same periodic structure. It demonstrates the existence of a more restricted type of spin-momentum locked wave generated by the transverse resonance between two photonic crystals in their bandgap, achievable via lateral sliding of finite thickness dielectric photonic crystals.

While the sliding interface structures enjoy the use of the widest fundamental bandgap resulting in an edge mode that is tightly bound to the interface, fabrication of a row of semi-circular or variably sliced holes at the interface poses a challenge, especially at the nanometer scale feature sizes that are required for operation at visible light frequencies. Furthermore, as the phase difference varies from the optimal condition for the transverse resonance, propagation length decreases leading to reduced intensity at the interface due to leakage.

In contrast, the large/small hole interface structures show highly robust spin-momentum locking due to their directional topological protection and are much easier to fabricate at optical frequencies. While the direction dependent bandgaps of the C_{4v} symmetric cells results in leakage if the wave propagates in directions of bandgap closure, these Zak phase devices are comparable in robustness performances to the conventional Chern number based PTIs in the direction of the calculated bandgap. This robustness is demonstrated and tested through the magic-T implementation which sees great applications in balanced mixers, microwave impedance bridges, duplexers, etc [45].

This chapter is based on "Spin-momentum locked interface modes based on transverse resonance and Zak phase in finite thickness dielectric slabs" by Shreya Singh, Dia'aaldin Bisharat and Dan Sievenpiper, *Under Submission*. The dissertation author was the primary author of this material.

Chapter 3

Photonic Topological Insulators as Aperture Antennas

3.1 Introduction

Antennas are essential components of all communication systems. Given the ubiquitous nature of device technology, individuals may be in proximity to or carry multiple antennas on their person at any given time. While antenna design constraints like gain, bandwidth, polarization, and size vary sharply based on the intended usage, low loss due to impedance mismatch remains a desirable outcome for all antenna engineers. Such mismatches may occur at the interface between the radiation volume and the antenna or the antenna and its feed and cause power that would ideally be radiated, to be reflected back to the feed. This results in a decrease in radiation efficiency, interference between the reflected and incoming wave and even possible component damage as the reflected wave travels back up the circuitry. Therefore, the design and implementation of an antenna matching network plays a very important role in the overall performance of any wireless device.

This chapter explores the utilization of spin Chern based topological surfaces as antennas.

While the use of topological structures as impedance matched feed elements for antennas arrays has been studied [46], it is mainly limited to pseudo-finite surfaces that require a breaking of the time reversal symmetry and are unaffected by the presence of a light cone. On the other hand, by simply adjusting the operating frequency of the proposed finite height topological device with respect to the light line, these plana topological metasurfaces can either support highly confined waves that can be used as aperture antennas or very loosely confined waves that have the potential to be used as leaky-wave antennas as will be discussed in chapter 4. For topological aperture antennas, the goal is minimizing impedance mismatch losses by the utilization of a metallic metasurface with the aforementioned topological properties of robust unidirectional propagation. Due to the strong spin-momentum locking, even upon encountering an impedance mismatch at the antenna aperture or the boundary between the guided mode and free space, reflection causing the wave to propagate back up the topological waveguide is not permitted. The energy is thus forced to radiate, making our proposed structure 'self-matched'. Furthermore, the bandwidth of this antenna is dependent on the width of the bandgap created during degeneracy breaking process which allows for self-matching over a wide band.

The subsequent sections detail the structure of the metasurface unit cell and the topological aperture antenna, followed by simulation data and a comparison to conventional aperture antennas like the rectangular waveguide aperture antenna and the planar Vivaldi antenna.

3.2 Device Structure

3.2.1 Structure of the metasurface PTI unit cell

The unit cell design for the aperture antenna is based on a C_{6v} symmetric hexagonal unit cell [20] as shown in figure 3.1(a). The hexagonal metallic patch supports a fundamental TE mode and is capacitive while its complementary hexagonal metallic grid supports a fundamental TM modes at the same frequency and is inductive. A hexagonal shape with a C_{6v} symmetry is

chosen as the geometry enforces a degeneracy in the dispersion diagram at the high symmetry K/K' points of the first Brillouin zone. As mentioned in chapter 1, for spin PTIs, multiple bands must intersect and create a degeneracy to allow for hybrid polarization modes to occur. By placing one layer above the other, at close distances, these electromagnetically complimentary or 'dual' metasurfaces experience a bi-anisotropic coupling. This bi-anisotropic coupling breaks opens the degeneracy point and creates a non-trivial bandgap for the structure. The closer the layers are to each other, the higher the coupling and the wider the opened bandgap.

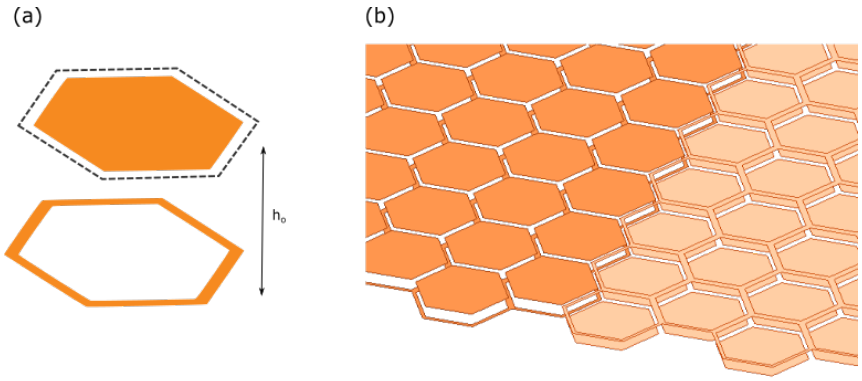

Figure 3.1: (a) Schematic of a single unit cell with a C_{6v} symmetric hexagonal patch and grid. (b) Creation of the interface by using a vertically (along the height separation axis) flipping of the metasurface. The darker pair of surfaces to the left of the interface has the hexagonal patches on the top and its inverse hexagonal grid on the bottom while the lighter pair of surfaces on the right reverses the order

Since the patch and the grid are complementary structures, all their modes overlap and have the same dispersion with the only difference being in the polarization of the modes. All TE modes of the patch will have TM field profiles for the grid while all TM modes of the patch will look like TE modes for the grid, at the exact same frequencies. This allows for the creation of hybrid modes or modes with 'pseudo-spins' that are a combination of the TE and TM modes as given by:

$$\Psi^{\pm} = \sqrt{\varepsilon_{\circ}}E \pm \sqrt{\mu_{\circ}}H \tag{3.1}$$

where Ψ^+ and Ψ^- are the two hybrid or pseudo-spin states, $\varepsilon_\circ$ and $\mu_\circ$ are the permittivity and permeability, and E and H are the total electric and magnetic fields respectively.

An interface can be created by placing this metasurface beside a flipped version (along the axis of the height separation between the layers) of itself. The modes that propagates at this interface are incredibly robust and show minimal scattering with along a zig-zag propagation path [20]. Figure 3.2 shows a zoomed in view of the dispersion curves around the K point of the first Brillouin zone. The grey regions represent the bulk modes, the area below the light line where the interface mode exists in the bandgap is in blue and the area above the light line where the interface mode exists is in pink. Operating the device in frequencies that lie in the blue region excites interface modes that are highly confined, making for great topological waveguides.

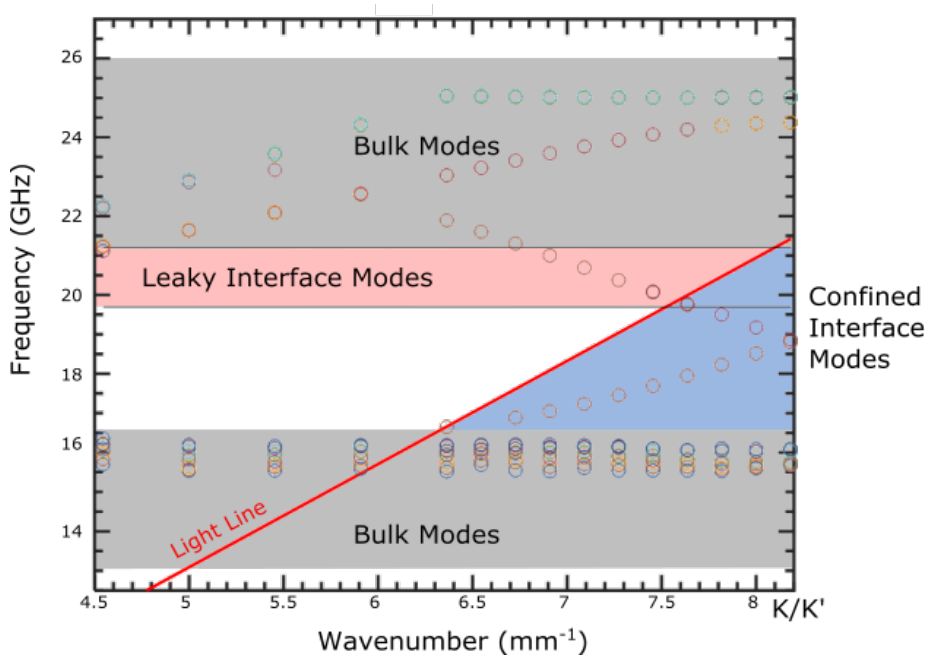

Figure 3.2: Eigenmode simulation around the K/K' point for a single row of the topological metasurface. The grey regions depict the bulk modes. The interface modes that traverse the bandgap are segregated based on their position w.r.t. to the red light line. The modes in the pink and blue shaded regions represent the frequencies where the topological interface modes are weakly and strongly confined to the surface respectively

3.2.2 Structure of the topological aperture antenna

The primary question that motivates a topological aperture antenna is what happens if a topological waveguide is abruptly truncated? Much like a conventional waveguide aperture, a topological waveguide supporting an interface mode can be created that ends in an abrupt truncation, creating an aperture to free space. To quantify the radiation performance, the feed excitation is an ordinary 50 Ω wave port at the opposite end of the truncation, with the return loss being measured at this feed point. The performance of this antenna, along with a few structural variations, is then measured in comparison to a typical rectangular waveguide aperture as well as a planar Vivaldi Antenna.

The full wave simulations were performed in Ansys HFSS and the periodicity of the hexagonal unit cells, width of the grid wires and top and bottom layer separation are 7 mm, $\sim$0.5 mm, and 0.127 mm respectively for operation in the 16-22 GHz range.

3.3 Results

Figure 3.3 depicts the color map of the fields along the length of the topological waveguide down to the aperture. Since the designs are fed at one end using an ordinary wave port, there is a mode profile mismatch between the photonic topological insulator (PTI) interface mode and wave port mode which causes the energy to scatter around the source region at length scales of approximately one wavelength. This can easily be mitigated by the selection of an appropriate feed of the twin line variety [47, 48]. As the excited energy couples into the PTI surface, a highly confined guided mode is observed, which is then abruptly truncated to free space. While the bulk of of the energy is radiated outwards at the truncation aperture, a portion clings onto the edges and weakly propagates down the side of the structure as seen in 3.3 (b). To minimize this leakage and increase radiation efficiency in the endfire direction, the top and bottom layers were shorted using vias (figure 3.3(c)). These vias or narrow metallic rods connect the patch and the

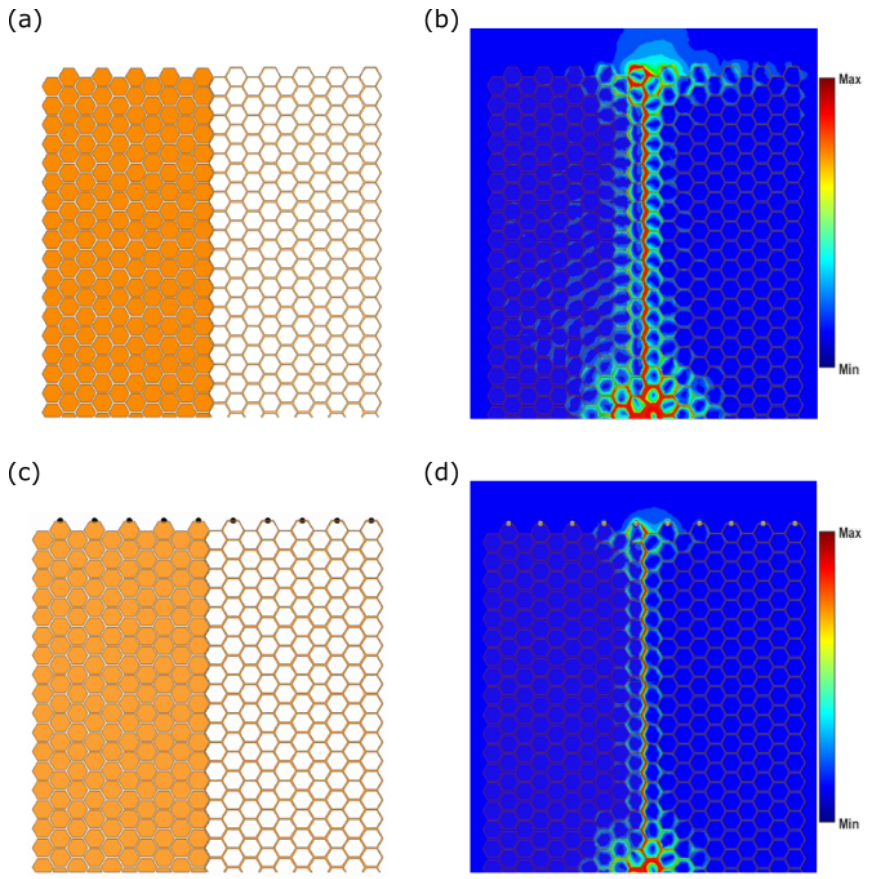

Figure 3.3: Electric field color maps of the topological antenna structures for four configurations. (a) Topological metasurface aperture antenna with abrupt truncation to free space and (b) its field profile showing edge leakage. (b) Topological metasurface aperture antenna with shorting pins at the truncation edge to reduce leakage with (d) the corresponding field magnitude plots. Energy spread located at the bottom is due to mode profile mismatch at the feed location

grid interface at the aperture and successfully minimize leakage as seen in figure 3.3(d). The vias erase the topological nature of the dual EM metallic metasurface at the edge and prevent any edge modes between air and the structure.

In order to compete with conventional aperture antennas in terms of physical size, the design was made much narrower by using only four sets of complementary unit cells on either side of the interface with vias at the truncation edge as depicted in figure 3.4(a). The vias prove more important for narrower structures as with narrow topological antennas without vias, the energy may not decay sufficiently across the length of the aperture, and instead loops around

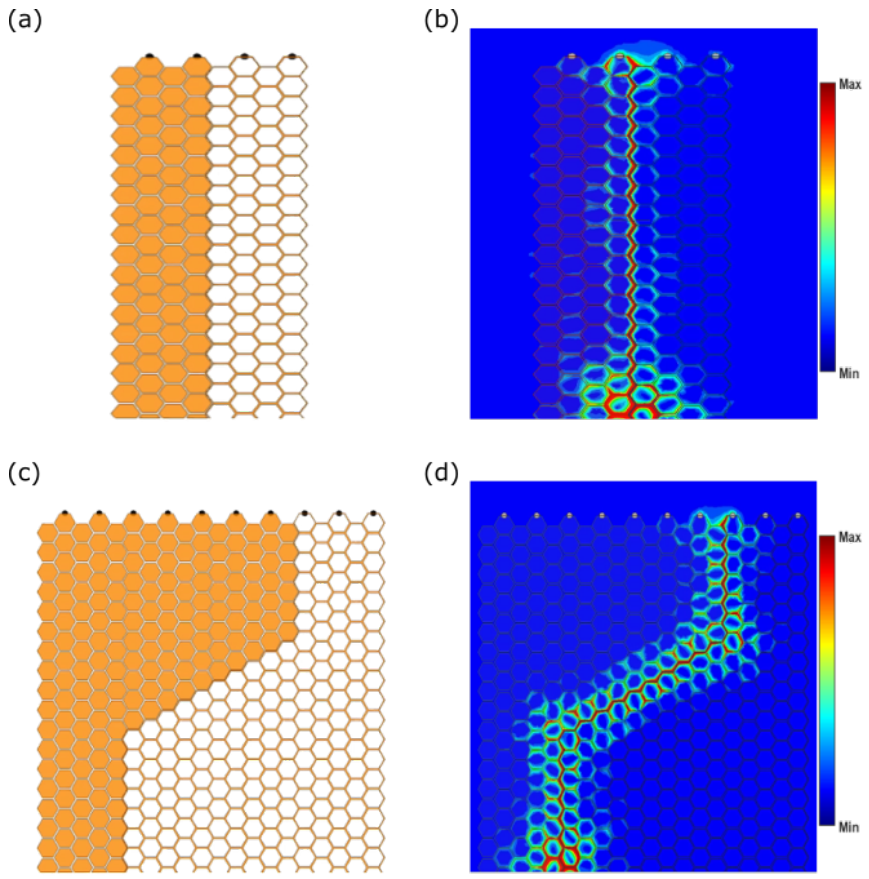

Figure 3.4: Electric field color maps of the topological antenna structures for four configurations. (a) Schematic and (b) field strength of a topological metasurface aperture antenna with reduce width and shorting pins. (c) Schematic and (d) field strength of a spin PTI metasurface aperture antenna with sharp bends in path. Energy spread located at the bottom is due to mode profile mismatch at the feed location

the structure to return back towards the source. The addition of vias, along with creating a more directive beam, has been seen to reduce the reflection coefficient in the chosen designs by 1-3 dB, especially in cases with narrow aperture widths. Detailed simulations also indicate the requirement of at least three hexagonal unit cells on either side of the interface to satisfy the Bloch's condition for periodic cells for this hexagonal metasurface, which is the limiting factor in aperture width. Furthermore, as expected of topological structures, the design is incredibly robust to reflections from sharp bends in the path as observed in figure 3.4(c) and (d).

Table 3.1 depicts the reflection coefficient (S11) and approximate bandwidth comparison

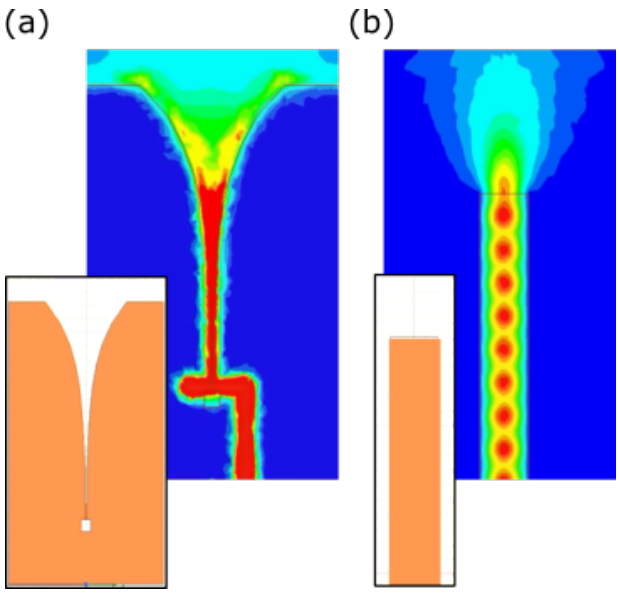

Figure 3.5: Typical structure and E field of a conventional (a) planar Vivaldi antenna and (b) rectangular waveguide aperture antenna

between conventional and topological aperture antennas. For conventional aperture antennas, optimized designs for a rectangular waveguide and a planar Vivaldi antenna (examples as seen in figure 3.5) were chosen with an operational bandwidth in the range of 16-23 GHz. For topological aperture antennas, the four cases depicted in figure 3.3 and 3.4 were picked: PTI truncated with and without shorting vias at the aperture edge, a narrower design with the shorting vias that reduces the number of unit cells on each side of the interface from ten to only four, and a design with two sharp bends in the propagation path. The data indicates that the topological antennas provide a comparable reflection coefficient to that of the waveguide aperture, showing great self-matching. Narrowing the design provides some performance degradation due to the reduced periodicity but still presents a voltage standing wave ratio (VSWR) value below 2. All topological antennas show lower reflection compared to a planar metallic Vivaldi antenna and their bandwidth can be further increased by either varying the thickness between the top and bottom hexagonal layers or by utilizing PTI designs with broader bandgaps.

An important test for input-matching robustness is a comparison of how the input reflection

Table 3.1: Comparison of reflection coefficient and bandwidth for topological aperture antennas and conventional aperture antennas in different configurations

Structure	Reflection Coefficient	Bandwidth
Waveguide Aperture Antenna	-18 dB	30%
Planar Vivaldi Antenna	-12 dB	32%
Waveguide Aperture to dielectric	-9.5 dB	22%
Topological Antenna (TA)	-16.5dB	27%
TA with shorting pins	-15 dB	27%
Narrow TA with shorting pins	-13 dB	27%
TA with sharp bends in path	-22 dB	27%
Narrow TA to dielectric	-12.5 dB	25%

changes as the radiation environment is modified. By allowing the antenna to radiate into a dielectric medium as opposed to vacuum, the impedance mismatch between the guided mode and radiated mode at the aperture is exacerbated. From table 3.1, a rectangular waveguide aperture that opens to a dielectric box placed in front of the aperture sees an increase of ~ 8.5 dB in the reflection loss, depicting how sensitive conventional antennas can be to changes in their radiation surroundings. On the other hand, the narrow topological aperture shows a minimal average increase of 0.5 dB across its bandwidth. The spin-momentum locked wave forbids any energy that is scattered from the dielectric box in front of the aperture from traveling back up the antenna, providing an excellent 'self-match' without the need for structural modifications or addition of lumped matching components.

Table 3.2: Comparison of physical dimensions of the two conventional aperture antennas and the best case of the topological aperture antenna

Structure	Width x Height
Waveguide Aperture Antenna	9 x 9 mm
Planar Vivaldi Antenna	33 x 1.36 mm [length=43mm]
Narrow TA with shorting pins	50 x 0.5 mm

Table 3.2 compares the physical dimension of the aperture width and height of the narrow topological aperture antenna to that of the Vivaldi and rectangular aperture antennas. The topological aperture antenna provides a narrower z-profile than both conventional apertures:

$\sim 94\%$ reduction in height with respect to a rectangular aperture. The height of the planar Vivaldi antenna is comparable to the height of the topological aperture antenna but unlike conventional waveguide apertures, the length of a Vivaldi antenna is an important dimension. The topological aperture antennas can be of any arbitrary length, above a minimum of three-four unit cells to allow for the validity of the energy band diagram that is derived from Bloch's theory for periodic structures, with no change in performance. This is in contrast to the Vivaldi antennas that must be long enough to allow for the flare that enables gradual impedance transformation and wide band operation and is conventionally of the order of two-four wavelengths or longer. While the antenna aperture is wider than both the conventional antennas, designs requiring fewer unit cells on each side or aperiodic PTIs can be considered. In each case, the topological apertures provide wide band radiation opportunities with a metasurface like planar topology while eliminating the need for impedance matching networks, which may be an attractive alternative for applications involving confined energy re-direction and/or re-radiation.

3.4 Conclusions

This chapter chiefly details the use of a spin photonic topological insulator, based on an induced bi-anisotropy of an electromagnetic dual metasurface, as an aperture antenna. It explores different configurations of aperture terminations and ways to minimize edge leakage by the additions of vias at the truncation edge. The vias provide a simple mechanism to break the the bi-anisotropic coupling between the layers and destroy the topological edge protection which prevents leakage at the interface between the PTI and free space. Narrower designs with only three to four unit cells on each side of the interface also suffice in creating aperture antennas with minimal performance degradation. A comparative study of of the reflection coefficients between the different topological designs and conventional aperture antennas shows comparable performance over a broad frequency range making topological aperture antennas an

attractive alternative with an added polarization degree of freedom. The self-matched nature of the topological designs makes them more resistant to changes in the environmental dielectric, signifying that these designs more robust and adaptable to operation in various surroundings without the need for modification. The bandwidth of the design can be easily tuned based on the choice of unit cell and the created bandgap. Contrary to the norm where increasing the dielectric height for patch antennas increases antenna bandwidth, increasing the layer separation for these PTI structures decreases the bi-anisotropic coupling and therefore, reduces the width of the bandgap and subsequently, operation bandwidth.

In terms of physical size, the use of a planar metasurface design provides a great reduction in antenna height which, when combined with the topological nature of the device, can allow for the creation of aperture antennas that conform to curved surfaces like a thin layered coating. These antennas also require no flaring for a gradual impedance transformation and wide bandwidth as compared to the other common industry standard planar aperture antenna, i.e., the Vivaldi antenna.

For operation at even higher frequencies or for mm wave devices, the structure can be scaled and the antenna has potential applications in wearable devices that bend and fit the body of the user. The polarization filtering between the two hybrid pseudo-spin modes can allow for separate up-link and down-link channels or even data multiplexing to increase the channel capacity and data transmission rates.

This chapter is based on "Topological antennas: Aperture radiators, leaky-wave surfaces, and orbital angular momentum beam generation" by Shreya Singh, Dia'aaldin Bisharat and Dan Sievenpiper, *Journal of Applied Physics*, 130(2):023101, 2021. The dissertation author was the primary author of this material.

Chapter 4

Orbital Angular Momentum beams using photonic topological insulators

4.1 Introduction

The emerging field of topological photonics has extended our capability to control and manipulate electromagnetic waves. Thus far, however, research has focused on realizing defect-immune waveguides for on-chip communication. Making a similar advancement for radiative components, which are crucial to the performance of wireless devices, could lead to a parallel impact on wireless communication and related technology.

Orbital angular momentum (OAM) beams are a class of vortex beams that are defined by an intensity null in center (along the beam axis) and a phase progression that is characterized by an angular variation in the azimuth direction. Mathematically, the phase variation is given by $e^{-jl\phi}$ where ϕ is the azimuth angle and l is the order of the OAM beam. It is also sometimes referred to as the topological OAM charge of the beam is analogous to the quantum number for orbital angular momentum in electrons. Figure 4.5 shows the characteristic amplitude and phase pattern of an OAM beam with charge $l = +9$, created by the proposed structure discussed in the

subsequent sections.

First introduced in 1992 [49], OAM beams, also sometimes referred to as helical beams, spiral beams, or vortex beams [50, 51, 52], were created by the conversion of Hermite-Gaussian laser modes to Leguerre-Gaussian laser modes using cylindrical lenses [49]. Since then many methods to create OAM beams have been developed that involve spiral phase plates [53, 54, 55], diffraction gratings [56, 57, 58], chromophores [59], nano-antennas [60], Q-plates [61, 62, 63], and computer holography [64, 65, 66]. At microwave frequencies, OAM beams have been created using complimentary metasurfaces [67], spiral metasurfaces [68], patch antennas [69], traveling waves in large loop antennas [70], and multi-layer polarizers [71]. This significant and on-going research into the generation of OAM beams is because angular momentum (both spin and orbital) adds additional degrees of freedom in electromagnetic wave manipulations. Some interesting applications that utilize this OAM degree of freedom include improvements in resolution and contrast in TEM imaging [72, 73], determining the handedness of chiral crystals [74, 75], studying Landau levels in free space [76, 77], and various methods of particle manipulation that involve an application of photonic torque for optical tweezers [78], optical wrenches [79], and optical particle sorters [80]. In the communication domain, multiplexing of different orders of OAM beams has led to an increase in channel capacity and higher data transmission [81, 82, 83, 84], encryption [85], photo-current detection for optical circuits [86] as well as the capability of receiving signals from outer space [87].

The subsequent sections, through simulations and experimentation, detail the use of a metasurface spin Chern photonic topological insulator (discussed in the previous chapter) operating in the leaky wave region above the light cone to create orbital angular beams with varying charges. Increasing frequency to just above the light line, the same device can be excited to produce spin-momentum locked waves that dissipate or radiate energy as they propagate along an interface. Similar to conventional leaky-wave structures, frequency dependent beam scanning can be observed. More interestingly, however, is the observation of spiral phase fronts of the

Poynting vector that resemble waves carrying orbital angular momentum (OAM). This method relies on using the robust, scattering-resistant modes of a PTI structure to allow an electromagnetic wave to propagate in a closed loop path without reflection at the bends and create a spiral phase pattern that shows an azimuth phase dependence. Since it based on the phase accumulated based on propagation path length, this technique also allows for an easy control over the sign and magnitude of the OAM beam order based on the PTI excitation method and variation in the physical and inverse space (wavenumber) lengths, respectively.

4.2 Operation above the light cone

Figure 4.1 re-highlights the spin PTI metasurface schematic and the dispersion diagram with an increased focus on operating in frequencies that lie in the region shaded in pink.

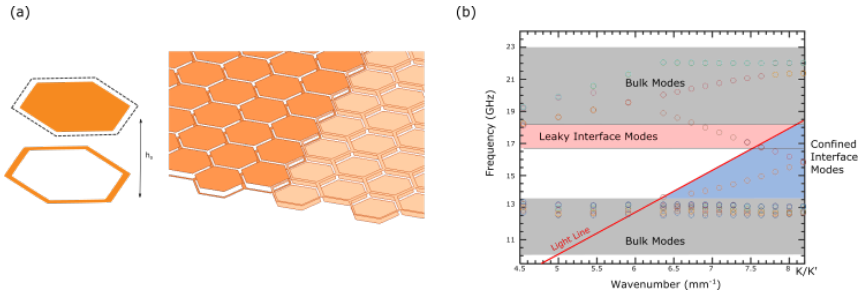

Figure 4.1: (a) Schematic of a single unit cell with a C_{6v} symmetric hexagonal patch and grid and creation of the interface by using a vertically (along the height separation axis) flipping of the metasurface. (b) Eigenmode simulation around the K/K' point for a single row of the topological metasurface. The interface modes that traverse the bandgap are segregated based on their position w.r.t. to the red light line. The modes in the pink and blue shaded regions represent the frequencies where the topological interface modes are weakly and strongly confined to the surface respectively.

Figure 4.2 shows the effects of operating the spin PTI metasurface at frequencies above the line line. While the topological protection ensures that the in-plane transverse confinement is maintained, the energy leaks or radiates above and below the surface, resulting in a decrease in propagation length. The unidirectional excitation in 4.2(b) ensure that the wave propagates in

only one direction and the intensity of the energy drops as the distance from the source increases. Figure 4.2(c) shows the drop in normalized power along the interface.

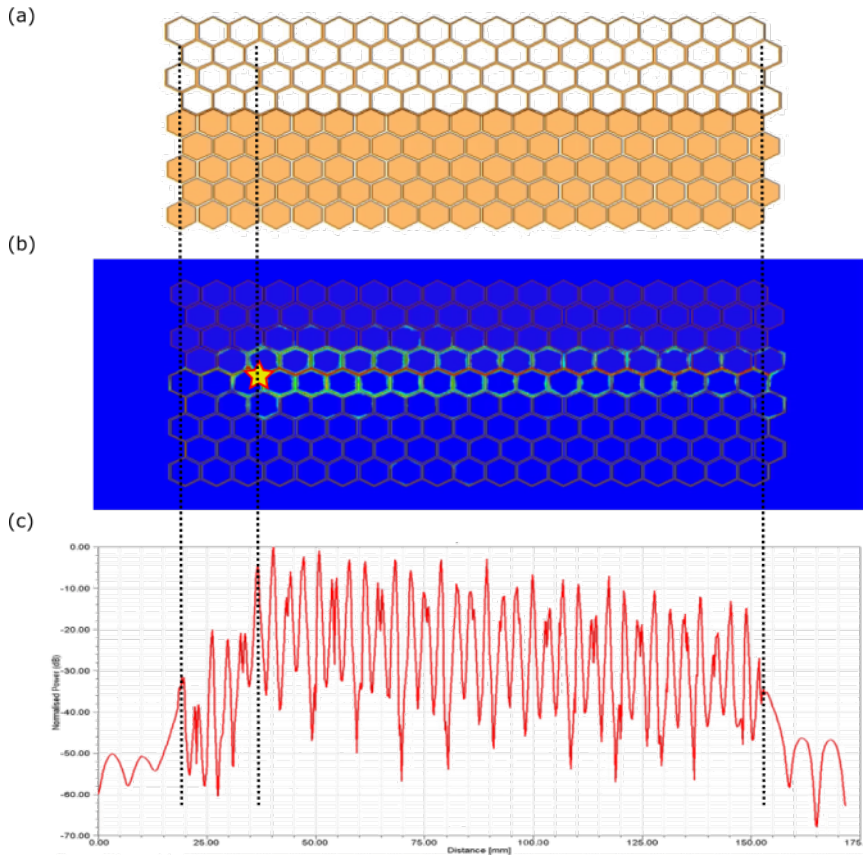

Figure 4.2: (a) Top view of the interface. (b) Energy dissipation as the wave propagates in a straight line. Star represents the location of the source. (c) Normalized power as a function of propagation length along the interface

Similar to the polarization-filtered topological aperture antennas discussed in the previous chapter, this structure can be used as a polarization-filtered leaky wave antenna. Figure 4.3 shows the frequency dependent beam scanning behaviour that is typical of all metasurface leaky wave antennas.

Since these leaky modes still exist in the bandgap and enjoy topological protection, they can be manipulated to travel in non-straight line paths with a significant immunity to back reflection, as long as polarization inversion does not occur. This allows for the creation of a

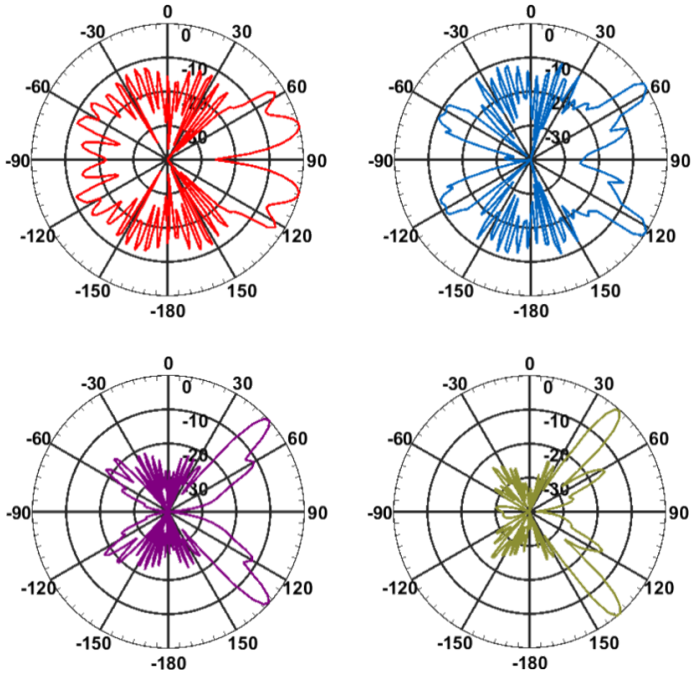

Figure 4.3: The structure shows beam scanning behaviour as the frequency is swept in the leaky-wave region with peaks at $\theta = \pm 76^\circ, \pm 58^\circ, \pm 48^\circ$ *and* $\pm 40^\circ$ in the direction of propagation

closed loop paths. Figure 4.4(a) shows a created hexagonal closed path. When the device is operated in the blue region from figure 4.1(b), highly confined waveguiding occurs, as is typical of PTI devices. The energy stays highly confined to the created hexagonal path and there is no noticeable decay in energy intensity as seen in figure 4.4(b). When the metasurface is coupled into at frequencies that lie in the pink region from figure 4.1(b), the energy intensity decreases as the wave propagates around the cloed hexagonal path as seen in figure 4.4(c). This lost energy is radiated into free space, both above and below the metasurface PTI. Lastly, when this surface is excited right at the edge of the pink and the upper grey section in figure 4.1(b), easy coupling to the bulk modes occurs and the energy leakage occurs both transversely and vertically.

When coupled into one of the hybrid pseudo-spin modes, the wave propagates in an anti-clockwise direction while when coupled into the other hybrid pseudo-spin mode supported by this spin PTI metasurface, the wave propagates in a clockwise direction as shown in figure

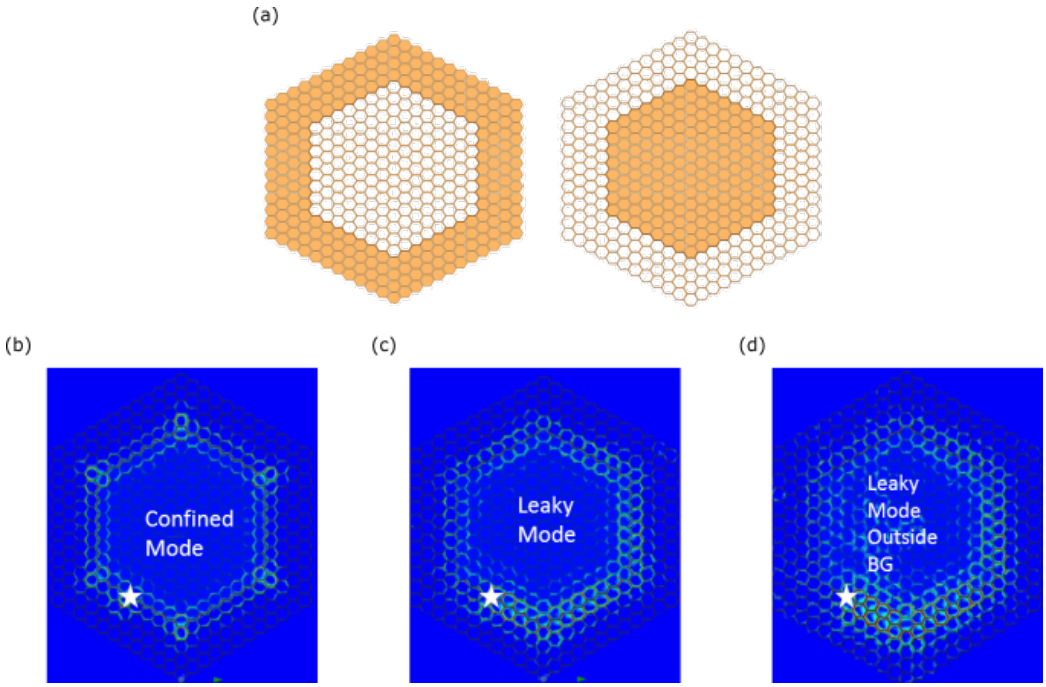

Figure 4.4: (a) Top view of the interface. (b) Energy dissipation as the wave propagates in a straight line. Star represents the location of the source. (c) Normalized power as a function of propagation length along the interface

4.5. Energy intensity decreases as the wave propagates at a frequency above the light line. The phase of the propagating interface mode is looped into a spiral pattern and the unidirectional and scattering resistant nature of the mode ensure no interference pattern is created and the spiral is undisturbed. The handedness of the spiral is decided by the direction of wave propagation and shows an azimuth variation that is typical of beams with orbital angular momentum (OAM).

4.3 Control of OAM beam order

The next step to creating OAM beams is to develop an ability to control them. Since this phenomenon is dependent on the phase that a wave accumulates as it travels around a closed loop path, OAM beam order or charge (l) can be controlled by varying the parameters that effect the wave phase. Given that any propagating plane wave can be described as:

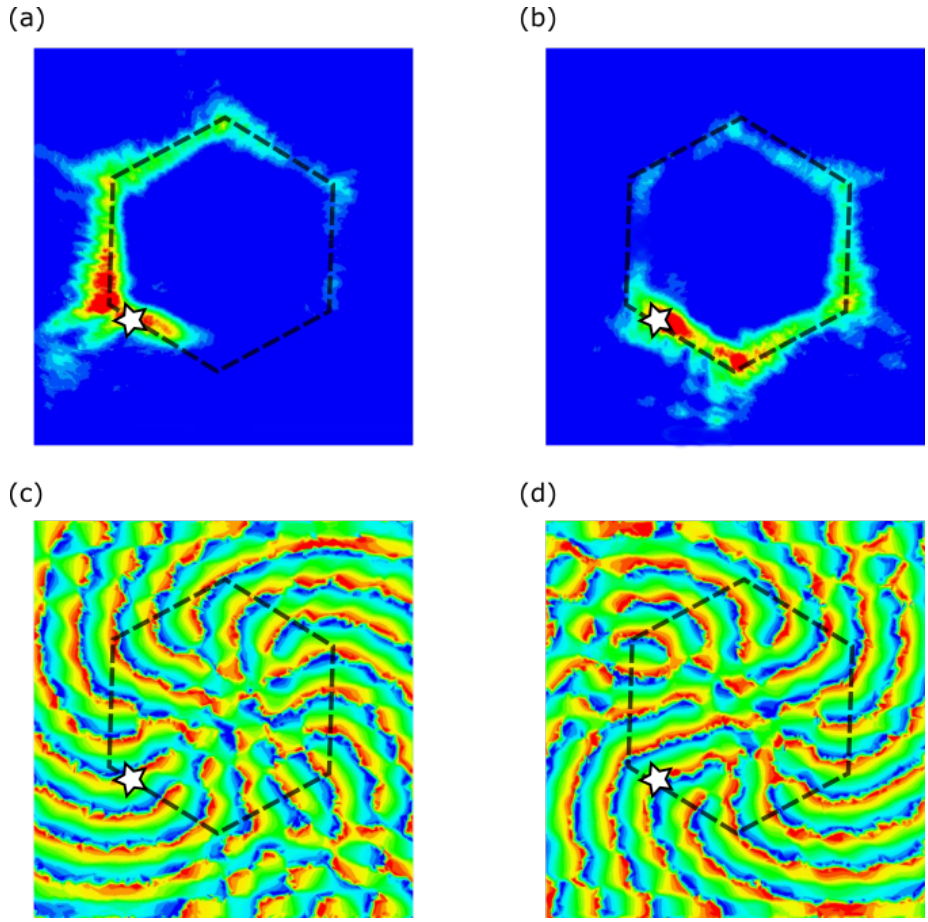

Figure 4.5: Magnitude of Poynting vector showing a wave propagating in the (a) clockwise and (b) anticlockwise direction. Since the wave is operating in the leaky wave region of the dispersion curves, intensity decreases as it propagates along the interface. Corresponding phase patterns showing an azimuth variation with (c) clockwise ($l = +16$) and (d) anticlockwise spirals ($l = -16$). Star shows the source location and the interface is given by the dotted black lines.

$$\mathbf{A}(\mathbf{x},t) = A_{\circ}(j\mathbf{kx} - j\omega t) \tag{4.1}$$

the phase of the wave depends primarily on two parameters: the physical length traveled and the electrical length or wave number. Modifying either of these parameters provides a way to control the OAM beam order that can be generated by this method of PTI excitation.

4.3.1 Modification of physical length

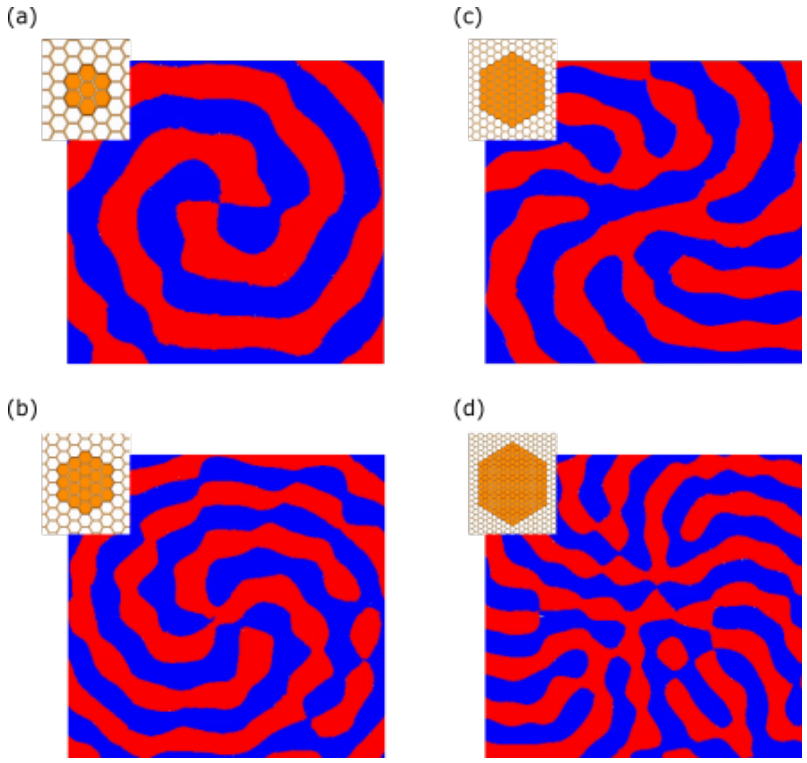

Figure 4.6: Change in OAM beam order as the path length varies. The inset image shows the top view of the spin PTI metasurface for generating beams with (a) $l = -2$, (b) $l = +4$, (c) $l = -9$, and (d) $l = +16$. The sign of the OAM charge is dependent on the polarization of the source excitement.

A simple means to modify the physical length of the device is by increasing the number of unit cells that make up the propagation path. As the wave travels longer distances, the number of times it wraps around in multiples of 2π increases, which increases the OAM charge. Much like its electronic analogue, the order of the OAM beam is quantized and only integer values of l are obtained. Figure 4.6 shows how the OAM charge can be varied by simply modifying the length of the interface. All of the OAM beam are plotted at the same frequency point with only a change in the number of unit cells that make up the interface. An excitation that couples into the hybrid pseudo-spin mode that rotates clockwise excites the mode propagating in the clockwise direction with a clockwise spiral phase and a positive OAM charge while flipping the phase of

the excitation causes it to couple to the opposite hybrid pseudo-spin interface mode, leading to a wave propagating in the anticlockwise direction with an anticlockwise phase and a negative OAM charge. The beam order can be visually calculated by the number of arms of the spiral and is always quantized. This techniques provides the ability to create arbitrarily high or low beam orders which lends a large degree of freedom and ease in adaptability for the creation of beams with varying OAM charges.

4.3.2 Modification of electrical length or wave number

The second quantity that can be modified to change phase accumulation is the wave number. While keeping the physical distance constant or using the sample device, sliding up and down on the frequency scale allows for a change in wave number. As long at the frequency change lies inside the leaky wave region where an interface mode exists, the wave will be radiative and the beam will possess an intrinsic OAM.

From figure 4.1(b), the portion of the interface mode that lies above the light line has a *negative* group velocity. As frequency increases, the value of the wave number k decreases, making the electrical length shorter. According to the phase relation $\phi = \mathbf{kx}$, this decrease in k, with a constant x, results in less phase accumulation and an overall decrease in OAM charge. The frequency sliding technique allows for a change in OAM order by $\pm$ 1 or $\pm$ 2 depending upon the width of the bandgap and the number frequencies where the leaky mode exists above the light cone. Figure 4.7 shows an example of the same surface creating OAM beams with $l = -7$, -8, and -9 as a function of frequency sliding on the same device. Each of these OAM charges has bandwidth of 2.8%, 4.3%, and 3% respectively. This method allows for easy multiplexing of adjacent order OAM beams that can be used in communication systems to increase data rates and channel capacity [84, 83, 82]. In this case, since the order of the OAM beams is solely based on changes in the electrical length, a similar small degree of freedom can also be obtained by placing a dielectric layer or bias-dependent surface above and below the spin PTI metasurface.

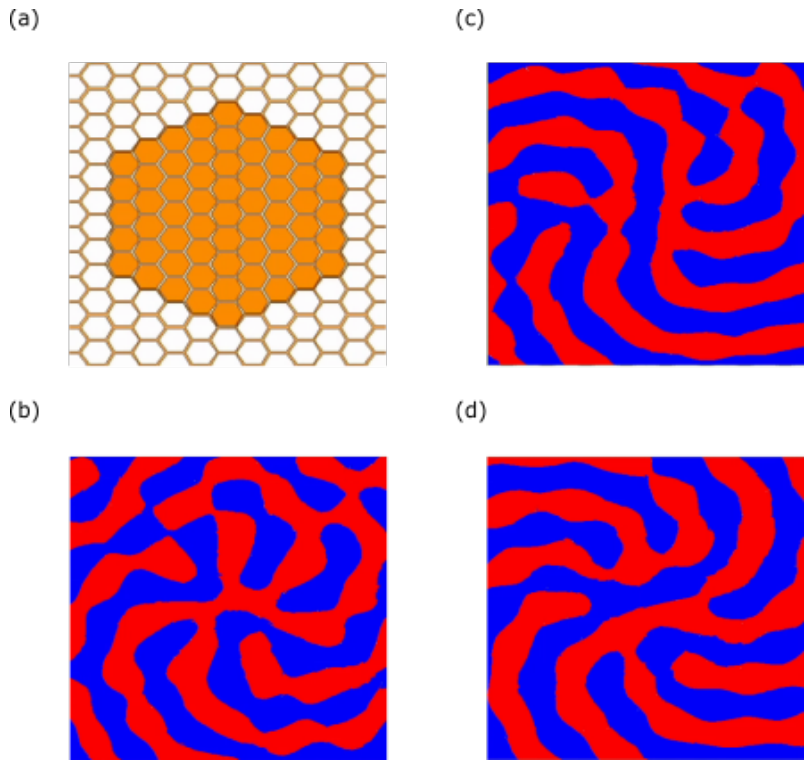

Figure 4.7: (a) Schematic showing the top view of the spin PTI metasurface used to generate OAM beams with (b)$l = -7$ at 18 GHz, (c) $l = -8$ at 17.25 GHz, and (d) $l = -9$ at 16.25 GHz. The sign of the OAM charge is dependent on the polarization of the source excitement.

The addition of dielectric toppers, liquid crystals or other temperature/voltage biased materials can lower the operating frequency and also allow the device to support two different orders of OAM beams at the same frequency through switching. Figure 4.8 shows a schematic and a comparative plot of the OAM charge on the same device with and without dielectric toppers (same thickness as the layer separation $\sim$ 5 mils). From figure 4.8(b), at an example frequency of 17 GHz, an OAM charge difference of 2 between the two states can be obtained with the possibility of even higher multiplexing using devices with wider bandgaps. The use of liquid crystals or other bias dependent surfaces should achieve a similar effect and allow for even easier charge multiplexing for the same sample based on a bias temperature/voltage to switch between the two OAM beams without the need for any physical modifications to the device.

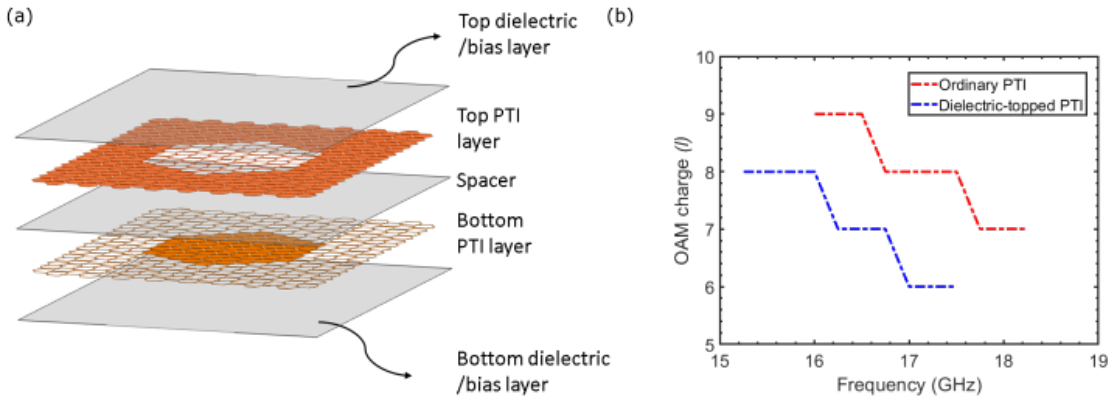

Figure 4.8: (a) Blown up view of the layers showing the sandwiching dielectric/bias layer and the spin PTI metasurface. (b) Difference in the OAM beam charge when the metasurface PTI is excited normally vs when the metasurface PTI is sandwiched between two thin dielectric layers ($\sim$ 5 mils each). The dielectric topped devices shows a reduction in operating frequency along with a drop in OAM charge

4.4 Measurements

All full wave simulations were performed using the Ansys HFSS electromagnetic suite and designed for operation in the 15-20 GHz microwave region. A dielectric spacer with relative permittivity of 10.9 was used (Rogers RT/duroid 5880), with the unit cell periodicity and the layer spacing (given by the dielectric height) being 7 mm and 0.127 mm ($\sim$ 5 mils), respectively.

Figure 4.9 shows a device manufactured for proof of concept with an OAM beam of order $+8$. The fabrication process of this technique involves only a basic two-layered pattering or etching of a dielectric printed circuit board. Most OAM beam generators involve the illumination of one side of a surface by a non-OAM beam which is then converted to a beam with intrinsic OAM on the other side of the surface. In contrast, this proposed structure is excited by a near field coupling and the OAM beam is radiated on both sides of the metasurface PTI.

Theoretically, the device can be coupled into in a variety of ways: 1) A source with a directional Poynting vector (along the interface) can be created by using an orthogonal configuration of electric and magnetic dipoles. Changing the phase of one of the dipoles flips the direction

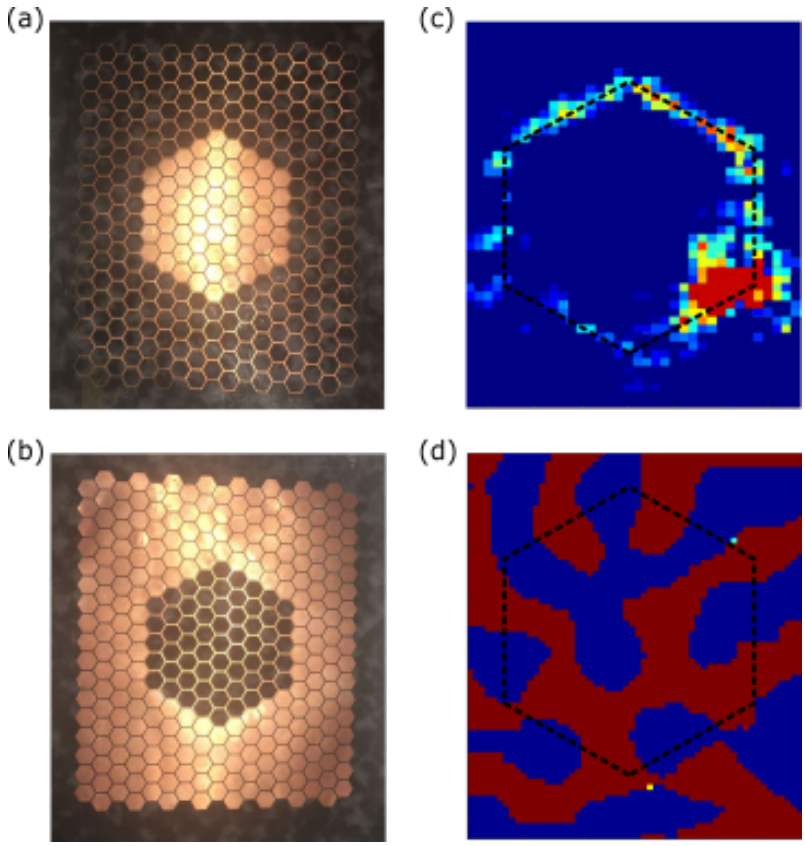

Figure 4.9: (a) Top and (b) bottom view of the fabricated spin PTI metasurface based on bi-anisotropic coupling. (c) Energy and (d) phase captured at a distance of 1.5 wavelengths away from the device surface showing an intensity null along the beam axis and a spiral azimuth phase variation for $l = +8$. The star give the location of the source

of the Poynting vector based on the right-hand rule and excites a wave propagating in the opposite direction. 2) A vertical electric and magnetic dipole placed at the same location excites the transverse electric and transverse magnetic modes that couple to create the hybrid pseudo-spin states that characterize this spin PTI structure. In-phase dipoles excite one hybrid mode while out-of-phase dipoles excite the opposite hybrid mode. It is important to note that both TE and TM modes must be excited with the same intensity for the creation of the hybrid pseudo-spin modes, which can be done by ensuring the magnitudes of the electric and magnetic dipole excitations are related by the impedance of free space. 3) A highly-directional excitation such a horn antenna can also be used to couple into the PTI device. For practical implementations, this last method

proves easiest and an absorber is placed around the directional excitation to suppresses any stray radiation that may result in propagation in the reverse direction. All simulation and measurement results are measured at distances greater than 1.5 wavelengths away from the metasurface PTI to ensure the capture of only radiated waves. However, phase measurements are highly sensitive to reflections from the edge of the fabricated board as well as radiation from source itself, and care must be taken to exclude or suppress these effects. While operating in frequencies below the light cone will also result in an azimuth phase variation, the waves are too tightly confined to the device surface to be of use as OAM beams.

4.5 Conclusion

As the use of electromagnetic energy possessing orbital angular momentum increases, simple methods to generate and control these beams are required. This chapter combines the concepts of spin photonic topological insulators and metasurface leaky wave antennas to achieve an easy technique to create OAM beams of any arbitrary order in the microwave region. While a sweeping control over beam order can be achieved by increasing or decreasing the number of unit cells that make up the propagation path, much finer control can be achieved by sliding up and down the interface mode frequencies that lie above the light cone. The frequency sweeping causes a variation in the wave number or electrical path length and can also be achieved by padding the surface with dielectric or bias dependent materials. The group velocity or slope of the interface mode determines if the OAM charge increases or decreases with a change in frequency.

The use of PTI surfaces guarantees an immunity to scattering due to propagation bends on closed paths which is an important factor in ensuring that no scattered energy couples into the hybrid pseudo-spin mode propagating in the reverse direction. Unwanted scattering results in an interference between the spiral phases generated by waves propagating in the clockwise and anticlockwise directions and a subsequent destruction of the inherent orbital angular momentum

of the beam. The finite height metasurface surface approach is also an important feature of the device as the creation of radiative OAM beams requires operation above the light cone which is not possible with infinite height PTI materials.

This chapter is based, in part, on "Topological antennas: Aperture radiators, leaky-wave surfaces, and orbital angular momentum beam generation" by Shreya Singh, Dia'aaldin Bisharat and Dan Sievenpiper, *Journal of Applied Physics*, 130(2):023101, 2021 **and** on "Generation and control of orbital angular momentum beams using metasurface photonic topological insulators" by Shreya Singh, Dia'aaldin Bisharat and Dan Sievenpiper, *In preparation*. The dissertation author was the primary author of both materials.

Chapter 5

Conclusion

5.1 PTIs and their applications

Photonic topological insulators represent an emerging area of scientific research into an exciting class of materials with many interesting properties. The physics behind these devices has been applied to both fermions and bosons and topological materials have been created in electronic [6, 7, 88, 89], acoustic [90, 91, 92], photonic [18, 19, 21] and other physical systems [93, 94]. These materials have the potential to revolutionize many areas in traditional electromagnetics design from highly robust cavities to increased waveguide stacking densities and device miniaturization [8].

With an explosion in techniques for the creation of microwave metasurfaces, there is great opportunity for practical new designs. By exploiting the robustness to disorder and amorphous construction as seen by the implementation of even non-periodic devices [95, 96], it is possible to enable self-assembly for large scale patterning. Current research on active [97, 98, 99] and modulated [100, 101, 102] topological metasurfaces may allow for fundamental bandwidth increases for absorbing or redirecting electromagnetic energy. Lastly, artificial intelligence and machine learning methods for rapid inverse design of metasurfaces [103, 104] are a promising

new avenue for many of the above technologies, and may find use in neuromorphic computing applications as well.

5.2 Summary

Chapter 1 provides an introduction to topological insulators with a quick glance at the many ways to create these materials through either the breaking of a time-reversal symmetry or through the breaking of a spatial inversion symmetry. It examines the difference between the PTI types as well as the differences in the band structures and the created interface modes. It also provides an introduction to topological invariants like the Chern number, which is obtained by the calculation of a quantized geometric phase called the Berry phase. The existence of a non-zero Berry phase implies that the material is capable of producing topologically protected edge states and the level of quantization decides the number of such states. Each of these states can be excited individually and usually possesses some sense of directionality that is extremely resistant to change. For Chern insulators, this is based on an electron spin. For spin and valley type PTIs, this directionality is dependent on the rotational nature of the modes.

Chapter 2 takes a closer look at interfaces modes through the lens of reduced dimensionality by calculating the 1D Berry phase of a 3D structure. Through simulations and test devices, it is observed that the existence of an incomplete bandgap can lead to lead to fairly robust and directional interface modes. It also explores an alternate, non-topological form of the interface mode that is created when bandgap materials with an equal but opposite reflection phase create an interface. The energy trapping states at the variable truncation of a photonic crystal, along with a transverse resonance established at the interface between two different materials, allows for high transverse confinement of the interface mode with long propagation lengths. The first interface mode is achieved by means of a ‘cell-sliding’ technique while the second interface mode, dependent on the calculation of a Zak phase, is based on a ‘cell-scaling’ technique to create a

large/small hole interface.

Chapter 3 uses a spin PTI metasurface based on bi-anisotropic coupling to create topological aperture antennas and perform a comparative study with conventional aperture radiators. Different variations of topological apertures are considered to minimize leakage and minimize device footprint. Size, reflection co-efficient and bandwidth comparisons are performed across various sets of topological antennas to determine the structure with the most optimal dimensions and radiation performance. The self-matched nature is further tested with a change in radiation environment and it's effect on the return loss is shown.

Finally, chapter 4 uses the same metallic spin PTI metasurface to generate beams possessing an intrinsic orbital angular momentum. Based on the location of the interface modes with respect to the light line, the device can be used for traditional wave guiding applications or as metasurface leaky wave antennas. The emitted beams show an intensity null along their axis along with an azimuth phase variation, marking them as waves possessing a quantized OAM charge. Methods to control this OAM beam charge are discussed with a focus on two approaches: varying the physical length and varying the electrical length, to provide for exciting opportunities of charge multiplexing.

5.3 Potential future work

With the devices based on Zak phase, there is significant ongoing research into similar structures with zero Berry curvature but non-zero Berry phase. While the Chern number approach does provide an ability to create waveguides with arbitrary bends, for fixed angle bends, Zak phase structures with incomplete bandgaps provide a simpler mathematical alternative. Investigations into other simpler C_{4v} geometries has shown the use of incomplete bandgap devices to create higher order topological modes with varying degrees of topological protection [105]. An exploration into more finite height height devices that do not require a complete bandgap to create

highly confined and robust interface modes could drastically increase the number of devices with easy fabrication steps that can be immediately deployed for real-world applications at microwave and optical frequencies.

Orbital angular momentum and the degree of freedom it provides for wave manipulation is an exciting current research prospect for many researchers in the electromagnetic domain. A natural extension of the work presented in the thesis is the implementation of bias based toppers or liquid crystals to achieve and measure real-time switching and multiplexing of different orders of OAM beams. A key challenge in this process remains efficient directional excitation and work is on-going to realize the same. Once efficient excitation has been achieved, he fabrication of sampled for use in an anechoic chamber to determine radiation efficiency, gain and main lobe angles to characterize the device efficacy as a leaky-wave antenna would be in order. Similar field tests of aperture antennas to quantify performance need further investigation as well.

Bibliography

[1] John H Conway, Heidi Burgiel, and Chaim Goodman-Strauss. *The symmetries of things*. CRC Press, 2016.

[2] Jeffrey R Weeks. *The shape of space*. Chapman and Hall/CRC, 2020.

[3] F Duncan M Haldane. Model for a quantum hall effect without landau levels: Condensed-matter realization of the“ parity anomaly”. *Physical review letters*, 61(18):2015, 1988.

[4] David J Thouless, Mahito Kohmoto, M Peter Nightingale, and Marcel den Nijs. Quantized hall conductance in a two-dimensional periodic potential. *Physical review letters*, 49(6):405, 1982.

[5] Charles L Kane and Eugene J Mele. Z 2 topological order and the quantum spin hall effect. *Physical review letters*, 95(14):146802, 2005.

[6] YL Chen, James G Analytis, J-H Chu, ZK Liu, S-K Mo, Xiao-Liang Qi, HJ Zhang, DH Lu, Xi Dai, and Zhong Fang. Experimental realization of a three-dimensional topological insulator, bi2te3. *science*, 325(5937):178–181, 2009.

[7] K Kuroda, M Ye, A Kimura, SV Eremeev, EE Krasovskii, EV Chulkov, Y Ueda, K Miyamoto, T Okuda, and K Shimada. Experimental realization of a three-dimensional topological insulator phase in ternary chalcogenide tlbise 2. *Physical review letters*, 105(14):146801, 2010.

[8] Dia'aaldin Bisharat, Robert Davis, Yun Zhou, Prabhakar Bandaru, and Dan Sievenpiper. Photonic topological insulators: A beginner's introduction [electromagnetic perspectives]. *IEEE Antennas and Propagation Magazine*, 63(3):112–124, 2021.

[9] Tomoki Ozawa, Hannah M Price, Alberto Amo, Nathan Goldman, Mohammad Hafezi, Ling Lu, Mikael C Rechtsman, David Schuster, Jonathan Simon, and Oded Zilberberg. Topological photonics. *Reviews of Modern Physics*, 91(1):015006, 2019.

[10] Xiao-Liang Qi and Shou-Cheng Zhang. Topological insulators and superconductors. *Reviews of Modern Physics*, 83(4):1057, 2011.

[11] Shivaramakrishnan Pancharatnam. Generalized theory of interference and its applications. *Proceedings of the Indian Academy of Sciences-Section A*, 44(6):398–417, 1956.

[12] Michael Victor Berry. Quantal phase factors accompanying adiabatic changes. *Proceedings of the Royal Society of London. A. Mathematical and Physical Sciences*, 392(1802):45–57, 1984.

[13] S Ali Hassani Gangaraj, Mário G Silveirinha, and George W Hanson. Berry phase, berry connection, and chern number for a continuum bianisotropic material from a classical electromagnetics perspective. *IEEE journal on multiscale and multiphysics computational techniques*, 2:3–17, 2017.

[14] Raymond Y Chiao and Yong-Shi Wu. Manifestations of berry's topological phase for the photon. *Physical review letters*, 57(8):933, 1986.

[15] Jens Von Bergmann and Hsingchi Von Bergmann. Foucault pendulum through basic geometry. *American Journal of Physics*, 75(10):888–892, 2007.

[16] Yasuhiro Hatsugai. Chern number and edge states in the integer quantum hall effect. *Physical review letters*, 71(22):3697, 1993.

[17] Zheng Wang, YD Chong, John D Joannopoulos, and Marin Soljačić. Reflection-free one-way edge modes in a gyromagnetic photonic crystal. *Physical review letters*, 100(1):013905, 2008.

[18] Alexander B Khanikaev, S Hossein Mousavi, Wang-Kong Tse, Mehdi Kargarian, Allan H MacDonald, and Gennady Shvets. Photonic topological insulators. *Nature materials*, 12(3):233–239, 2013.

[19] Tzuhsuan Ma, Alexander B Khanikaev, S Hossein Mousavi, and Gennady Shvets. Guiding electromagnetic waves around sharp corners: topologically protected photonic transport in metawaveguides. *Physical review letters*, 114(12):127401, 2015.

[20] Dia'aaldin J Bisharat and Daniel F Sievenpiper. Electromagnetic-dual metasurfaces for topological states along a 1d interface. *Laser & Photonics Reviews*, 13(10):1900126, 2019.

[21] Tzuhsuan Ma and Gennady Shvets. All-si valley-hall photonic topological insulator. *New Journal of Physics*, 18(2):025012, 2016.

[22] Chen Fang, Matthew J Gilbert, and B Andrei Bernevig. Bulk topological invariants in noninteracting point group symmetric insulators. *Physical Review B*, 86(11):115112, 2012.

[23] María Blanco de Paz, Chiara Devescovi, Geza Giedke, Juan José Saenz, Maia G Vergniory, Barry Bradlyn, Dario Bercioux, and Aitzol García-Etxarri. Tutorial: computing topological invariants in 2d photonic crystals. *Advanced Quantum Technologies*, 3(2):1900117, 2020.

[24] Chenyang Wang, Hongyu Zhang, Hongyi Yuan, Jinrui Zhong, and Cuicui Lu. Universal numerical calculation method for the berry curvature and chern numbers of typical topological photonic crystals. *Frontiers of Optoelectronics*, pages 1–16, 2020.

[25] Timothy Innes, David Spivey, and Kevin Igoe. Optical communications cables utilizing topological insulators as optical fiber cores, August 6 2019. US Patent 10,371,910.

[26] Xueqin Huang, Meng Xiao, Zhao-Qing Zhang, and Che Ting Chan. Sufficient condition for the existence of interface states in some two-dimensional photonic crystals. *Physical Review B*, 90(7):075423, 2014.

[27] Wen Sheng Gao, Meng Xiao, Che Ting Chan, and Wing Yim Tam. Determination of zak phase by reflection phase in 1d photonic crystals. *Optics Letters*, 40(22):5259–5262, 2015.

[28] Nathan Marcuvitz. *Waveguide handbook*. Number 21. Iet, 1951.

[29] Michela F Picardi, Anatoly V Zayats, and Francisco J Rodríguez-Fortuño. Janus and huygens dipoles: near-field directionality beyond spin-momentum locking. *Physical review letters*, 120(11):117402, 2018.

[30] Konstantin Y Bliokh, Aleksandr Y Bekshaev, and Franco Nori. Extraordinary momentum and spin in evanescent waves. *Nature communications*, 5(1):1–8, 2014.

[31] Todd Van Mechelen and Zubin Jacob. Universal spin-momentum locking of evanescent waves. *Optica*, 3(2):118–126, 2016.

[32] Zhida Song, Tiantian Zhang, Zhong Fang, and Chen Fang. Quantitative mappings between symmetry and topology in solids. *Nature communications*, 9(1):1–7, 2018.

[33] Yuting Yang, Tao Xu, Yun Fei Xu, and Zhi Hong Hang. Zak phase induced multiband waveguide by two-dimensional photonic crystals. *Optics Letters*, 42(16):3085–3088, 2017.

[34] Xueqin Huang, Yuting Yang, Zhi Hong Hang, Zhao-Qing Zhang, and Che Ting Chan. Geometric phase induced interface states in mutually inverted two-dimensional photonic crystals. *Physical Review B*, 93(8):085415, 2016.

[35] John D Joannopoulos, RD Meade, and Joshua N Winn. Photonic crystals. *Molding the flow of light*, 1995.

[36] Xiao-Dong Chen, Fu-Li Zhao, Min Chen, and Jian-Wen Dong. Valley-contrasting physics in all-dielectric photonic crystals: Orbital angular momentum and topological propagation. *Physical Review B*, 96(2):020202, 2017.

[37] Feng Liu and Katsunori Wakabayashi. Novel topological phase with a zero berry curvature. *Physical review letters*, 118(7):076803, 2017.

[38] Feng Liu, Hai-Yao Deng, and Katsunori Wakabayashi. Topological photonic crystals with zero berry curvature. *Physical Review B*, 97(3):035442, 2018.

[39] J Zak. Berrys phase for energy bands in solids. *Physical review letters*, 62(23):2747, 1989.

[40] Marcos Atala, Monika Aidelsburger, Julio T Barreiro, Dmitry Abanin, Takuya Kitagawa, Eugene Demler, and Immanuel Bloch. Direct measurement of the zak phase in topological bloch bands. *Nature Physics*, 9(12):795–800, 2013.

[41] Pierre Delplace, D Ullmo, and G Montambaux. Zak phase and the existence of edge states in graphene. *Physical Review B*, 84(19):195452, 2011.

[42] Mehul P Makwana and Richard V Craster. Designing multidirectional energy splitters and topological valley supernetworks. *Physical Review B*, 98(23):235125, 2018.

[43] Zhixia Xu, Xiaoxing Yin, and Daniel F Sievenpiper. Adiabatic mode-matching techniques for coupling between conventional microwave transmission lines and one-dimensional impedance-interface waveguides. *Physical Review Applied*, 11(4):044071, 2019.

[44] Robert J Davis, Dia'aaldin J Bisharat, and Daniel F Sievenpiper. Classical-to-topological transmission line couplers. *Applied Physics Letters*, 118(13):131102, 2021.

[45] Carol Gray Montgomery, Robert Henry Dicke, and Edward M Purcell. *Principles of microwave circuits*. Number 25. Iet, 1987.

[46] Yaakov Lumer and Nader Engheta. Topological insulator antenna arrays. *ACS Photonics*, 7(8):2244–2251, 2020.

[47] Zhixia Xu, Xiaoxing Yin, and Daniel F Sievenpiper. Adiabatic mode-matching techniques for coupling between conventional microwave transmission lines and one-dimensional impedance-interface waveguides. *Physical Review Applied*, 11(4):044071, 2019.

[48] Robert Davis, Dia'aaldin J Bisharat, and Daniel F Sievenpiper. Efficient transition from a planar transmission to a topological line wave. *IEEE Antennas and Propagation Symposium*, 2020.

[49] Les Allen, Marco W Beijersbergen, RJC Spreeuw, and JP Woerdman. Orbital angular momentum of light and the transformation of laguerre-gaussian laser modes. *Physical review A*, 45(11):8185, 1992.

[50] Miles Padgett, Johannes Courtial, and Les Allen. Light's orbital angular momentum. *Physics today*, 57(5):35–40, 2004.

[51] Shilie Zheng, Yiling Chen, Zhuofan Zhang, Xiaofeng Jin, Hao Chi, Xianmin Zhang, and Zhi Ning Chen. Realization of beam steering based on plane spiral orbital angular momentum wave. *IEEE Transactions on Antennas and Propagation*, 66(3):1352–1358, 2017.

[52] Yi-Dong Liu, Chunqing Gao, Mingwei Gao, Xiaoqing Qi, and Horst Weber. Superposition and detection of two helical beams for optical orbital angular momentum communication. *Optics Communications*, 281(14):3636–3639, 2008.

[53] MW Beijersbergen, RPC Coerwinkel, M Kristensen, and JP Woerdman. Helical-wavefront laser beams produced with a spiral phaseplate. *Optics communications*, 112(5-6):321–327, 1994.

[54] Gabriel Biener, Avi Niv, Vladimir Kleiner, and Erez Hasman. Formation of helical beams by use of pancharatnam–berry phase optical elements. *Optics letters*, 27(21):1875–1877, 2002.

[55] Dmitry Zelenchuk and Vincent Fusco. Split-ring fss spiral phase plate. *IEEE Antennas and Wireless Propagation Letters*, 12:284–287, 2013.

[56] V Yu Bazhenov, MS Soskin, and MV Vasnetsov. Screw dislocations in light wavefronts. *Journal of Modern Optics*, 39(5):985–990, 1992.

[57] Zeev Bomzon, Gabriel Biener, Vladimir Kleiner, and Erez Hasman. Radially and azimuthally polarized beams generated by space-variant dielectric subwavelength gratings. *Optics letters*, 27(5):285–287, 2002.

[58] G Machavariani, Y Lumer, I Moshe, A Meir, and S Jackel. Spatially-variable retardation plate for efficient generation of radially-and azimuthally-polarized beams. *Optics Communications*, 281(4):732–738, 2008.

[59] Mathew D Williams, Matt M Coles, Kamel Saadi, David S Bradshaw, and David L Andrews. Optical vortex generation from molecular chromophore arrays. *Physical review letters*, 111(15):153603, 2013.

[60] Ebrahim Karimi, Sebastian A Schulz, Israel De Leon, Hammam Qassim, Jeremy Upham, and Robert W Boyd. Generating optical orbital angular momentum at visible wavelengths using a plasmonic metasurface. *Light: Science & Applications*, 3(5):e167–e167, 2014.

[61] Ebrahim Karimi, Bruno Piccirillo, Eleonora Nagali, Lorenzo Marrucci, and Enrico Santamato. Efficient generation and sorting of orbital angular momentum eigenmodes of light by thermally tuned q-plates. *Applied Physics Letters*, 94(23):231124, 2009.

[62] P Gregg, M Mirhosseini, A Rubano, L Marrucci, E Karimi, RW Boyd, and S Ramachandran. Q-plates as higher order polarization controllers for orbital angular momentum modes of fiber. *Optics letters*, 40(8):1729–1732, 2015.

[63] Bruno Piccirillo, Vincenzo DAmbrosio, Sergei Slussarenko, Lorenzo Marrucci, and Enrico Santamato. Photon spin-to-orbital angular momentum conversion via an electrically tunable q-plate. *Applied Physics Letters*, 97(24):241104, 2010.

[64] Haoran Ren, Xinyuan Fang, Jaehyuck Jang, Johannes Bürger, Junsuk Rho, and Stefan A Maier. Complex-amplitude metasurface-based orbital angular momentum holography in momentum space. *Nature Nanotechnology*, 15(11):948–955, 2020.

[65] Hongqiang Zhou, Basudeb Sain, Yongtian Wang, Christian Schlickriede, Ruizhe Zhao, Xue Zhang, Qunshuo Wei, Xiaowei Li, Lingling Huang, and Thomas Zentgraf. Polarization-encrypted orbital angular momentum multiplexed metasurface holography. *ACS nano*, 14(5):5553–5559, 2020.

[66] S Chávez-Cerda, MJ Padgett, I Allison, GHC New, Julio C Gutiérrez-Vega, AT ONeil, I MacVicar, and J Courtial. Holographic generation and orbital angular momentum of high-order mathieu beams. *Journal of Optics B: Quantum and Semiclassical Optics*, 4(2):S52, 2002.

[67] Menglin LN Chen, Li Jun Jiang, and EI Wei. Ultrathin complementary metasurface for orbital angular momentum generation at microwave frequencies. *IEEE Transactions on Antennas and Propagation*, 65(1):396–400, 2016.

[68] Li Cheng, Wei Hong, and Zhang-Cheng Hao. Generation of electromagnetic waves with arbitrary orbital angular momentum modes. *Scientific reports*, 4(1):1–5, 2014.

[69] Mirko Barbuto, Fabrizio Trotta, Filiberto Bilotti, and Alessandro Toscano. Circular polarized patch antenna generating orbital angular momentum. *Progress In Electromagnetics Research*, 148:23–30, 2014.

[70] Shilie Zheng, Xiaonan Hui, Xiaofeng Jin, Hao Chi, and Xianmin Zhang. Transmission characteristics of a twisted radio wave based on circular traveling-wave antenna. *IEEE Transactions on Antennas and Propagation*, 63(4):1530–1536, 2015.

[71] Yiling Chen, Shilie Zheng, Yue Li, Xiaonan Hui, Xiaofeng Jin, Hao Chi, and Xianmin Zhang. A flat-lensed spiral phase plate based on phase-shifting surface for generation of millimeter-wave oam beam. *IEEE Antennas and Wireless Propagation Letters*, 15:1156–1158, 2015.

[72] Armand Béché, R Juchtmans, and J Verbeeck. Efficient creation of electron vortex beams for high resolution stem imaging. *Ultramicroscopy*, 178:12–19, 2017.

[73] Hiroki Minoda, Tatsuhiro Okabe, and Hirofumi Iijima. Contrast enhancement in the phase plate transmission electron microscopy using an objective lens with a long focal length. *Journal of electron microscopy*, 60(5):337–343, 2011.

[74] Robert P Cameron, Jörg B Götte, Stephen M Barnett, and Alison M Yao. Chirality and the angular momentum of light. *Philosophical Transactions of the Royal Society A: Mathematical, Physical and Engineering Sciences*, 375(2087):20150433, 2017.

[75] Roeland Juchtmans, Armand Béché, Artem Abakumov, Maria Batuk, and Jo Verbeeck. Using electron vortex beams to determine chirality of crystals in transmission electron microscopy. *Physical Review B*, 91(9):094112, 2015.

[76] Konstantin Y Bliokh, Peter Schattschneider, Jo Verbeeck, and Franco Nori. Electron vortex beams in a magnetic field: A new twist on landau levels and aharonov-bohm states. *Physical Review X*, 2(4):041011, 2012.

[77] Konstantin Y Bliokh, Igor P Ivanov, Giulio Guzzinati, Laura Clark, Ruben Van Boxem, Armand Béché, Roeland Juchtmans, Miguel A Alonso, Peter Schattschneider, and Franco Nori. Theory and applications of free-electron vortex states. *Physics Reports*, 690:1–70, 2017.

[78] Mindaugas Gecevičius, Rokas Drevinskas, Martynas Beresna, and Peter G Kazansky. Single beam optical vortex tweezers with tunable orbital angular momentum. *Applied Physics Letters*, 104(23):231110, 2014.

[79] NB Simpson, L Allen, and MJ Padgett. Optical tweezers and optical spanners with laguerre–gaussian modes. *journal of modern optics*, 43(12):2485–2491, 1996.

[80] Valeriia Bobkova, Jan Stegemann, Ramon Droop, Eileen Otte, and Cornelia Denz. Optical grinder: sorting of trapped particles by orbital angular momentum. *Optics Express*, 29(9):12967–12975, 2021.

[81] Alan E Willner, Yongxiong Ren, Guodong Xie, Yan Yan, Long Li, Zhe Zhao, Jian Wang, Moshe Tur, Andreas F Molisch, and Solyman Ashrafi. Recent advances in high-capacity free-space optical and radio-frequency communications using orbital angular momentum multiplexing. *Philosophical Transactions of the Royal Society A: Mathematical, Physical and Engineering Sciences*, 375(2087):20150439, 2017.

[82] Julio T Barreiro, Tzu-Chieh Wei, and Paul G Kwiat. Beating the channel capacity limit for linear photonic superdense coding. *Nature physics*, 4(4):282–286, 2008.

[83] Graham Gibson, Johannes Courtial, Miles J Padgett, Mikhail Vasnetsov, Valeriy Pasko, Stephen M Barnett, and Sonja Franke-Arnold. Free-space information transfer using light beams carrying orbital angular momentum. *Optics express*, 12(22):5448–5456, 2004.

[84] Yan Yan, Guodong Xie, Martin PJ Lavery, Hao Huang, Nisar Ahmed, Changjing Bao, Yongxiong Ren, Yinwen Cao, Long Li, and Zhe Zhao. High-capacity millimetre-wave communications with orbital angular momentum multiplexing. *Nature communications*, 5(1):1–9, 2014.

[85] Xinyuan Fang, Haoran Ren, and Min Gu. Orbital angular momentum holography for high-security encryption. *Nature Photonics*, 14(2):102–108, 2020.

[86] Zhurun Ji, Wenjing Liu, Sergiy Krylyuk, Xiaopeng Fan, Zhifeng Zhang, Anlian Pan, Liang Feng, Albert Davydov, and Ritesh Agarwal. Photocurrent detection of the orbital angular momentum of light. *Science*, 368(6492):763–767, 2020.

[87] Fabrizio Tamburini, Bo Thidé, and Massimo Della Valle. Measurement of the spin of the m87 black hole from its observed twisted light. *Monthly Notices of the Royal Astronomical Society: Letters*, 492(1):L22–L27, 2020.

[88] Chong Wang, Andrew C Potter, and T Senthil. Classification of interacting electronic topological insulators in three dimensions. *Science*, 343(6171):629–631, 2014.

[89] Cui-Zu Chang, Jinsong Zhang, Xiao Feng, Jie Shen, Zuocheng Zhang, Minghua Guo, Kang Li, Yunbo Ou, Pang Wei, and Li-Li Wang. Experimental observation of the quantum anomalous hall effect in a magnetic topological insulator. *Science*, 340(6129):167–170, 2013.

[90] Cheng He, Xu Ni, Hao Ge, Xiao-Chen Sun, Yan-Bin Chen, Ming-Hui Lu, Xiao-Ping Liu, and Yan-Feng Chen. Acoustic topological insulator and robust one-way sound transport. *Nature physics*, 12(12):1124–1129, 2016.

[91] Haoran Xue, Yahui Yang, Fei Gao, Yidong Chong, and Baile Zhang. Acoustic higher-order topological insulator on a kagome lattice. *Nature materials*, 18(2):108–112, 2019.

[92] Degang Zhao, Meng Xiao, Chi Wai Ling, Che Ting Chan, and Kin Hung Fung. Topological interface modes in local resonant acoustic systems. *Physical Review B*, 98(1):014110, 2018.

[93] Yun Zhou, Prabhakar R Bandaru, and Daniel F Sievenpiper. Quantum-spin-hall topological insulator in a spring-mass system. *New Journal of Physics*, 20(12):123011, 2018.

[94] Hiromasa Wakao, Tsuneya Yoshida, Hiromu Araki, Tomonari Mizoguchi, and Yasuhiro Hatsugai. Higher-order topological phases in a spring-mass model on a breathing kagome lattice. *Physical Review B*, 101(9):094107, 2020.

[95] Noah P Mitchell, Lisa M Nash, Daniel Hexner, Ari M Turner, and William TM Irvine. Amorphous topological insulators constructed from random point sets. *Nature Physics*, 14(4):380–385, 2018.

[96] Peiheng Zhou, Gui-Geng Liu, Xin Ren, Yihao Yang, Haoran Xue, Lei Bi, Longjiang Deng, Yidong Chong, and Baile Zhang. Photonic amorphous topological insulator. *Light: Science & Applications*, 9(1):1–8, 2020.

[97] Yasutomo Ota, Kenta Takata, Tomoki Ozawa, Alberto Amo, Zhetao Jia, Boubacar Kante, Masaya Notomi, Yasuhiko Arakawa, and Satoshi Iwamoto. Active topological photonics. *Nanophotonics*, 9(3):547–567, 2020.

[98] Miguel A Bandres, Steffen Wittek, Gal Harari, Midya Parto, Jinhan Ren, Mordechai Segev, Demetrios N Christodoulides, and Mercedeh Khajavikhan. Topological insulator laser: Experiments. *Science*, 359(6381), 2018.

[99] Anton Souslov, Benjamin C Van Zuiden, Denis Bartolo, and Vincenzo Vitelli. Topological sound in active-liquid metamaterials. *Nature Physics*, 13(11):1091–1094, 2017.

[100] Sebabrata Mukherjee, Alexander Spracklen, Manuel Valiente, Erika Andersson, Patrik Öhberg, Nathan Goldman, and Robert R Thomson. Experimental observation of anomalous topological edge modes in a slowly driven photonic lattice. *Nature communications*, 8(1):1–7, 2017.

[101] Matheus IN Rosa, Raj Kumar Pal, José RF Arruda, and Massimo Ruzzene. Edge states and topological pumping in spatially modulated elastic lattices. *Physical review letters*, 123(3):034301, 2019.

[102] Emanuele Riva, Matheus IN Rosa, and Massimo Ruzzene. Edge states and topological pumping in stiffness-modulated elastic plates. *Physical Review B*, 101(9):094307, 2020.

[103] Joaquin F Rodriguez-Nieva and Mathias S Scheurer. Identifying topological order through unsupervised machine learning. *Nature Physics*, 15(8):790–795, 2019.

[104] NL Holanda and MAR Griffith. Machine learning topological phases in real space. *Physical Review B*, 102(5):054107, 2020.

[105] Bi-Ye Xie, Hong-Fei Wang, Hai-Xiao Wang, Xue-Yi Zhu, Jian-Hua Jiang, Ming-Hui Lu, and Yan-Feng Chen. Second-order photonic topological insulator with corner states. *Physical Review B*, 98(20):205147, 2018.